STRATEGIES TO ENGINEER THE CAPTURE OF A MEMBER OF A BINARY ASTEROID PAIR USING THE PLANAR PARABOLIC RESTRICTED THREE-BODY PROBLEM

Xiaoyu Liu[1], Colin McInnes[2], Matteo Ceriotti[3]

ABSTRACT

This paper investigates two strategies to engineer the capture of one member of a binary asteroid pair by a planetary body after close encounter with that planetary body. It is assumed that the binary pair consists of a smaller minor asteroid in orbit about a larger main asteroid, which encounters a planetary body. In order to develop an engineering model of the problem, first we neglect the mass of the smaller minor asteroid in the binary pair and approximate the model as planar parabolic restricted three-body problem (PPRTBP). Second, the related regularised dynamical equations for the problem are developed. An approximate analytical solution to the problem is then obtained for motion in the vicinity of the main asteroid using the regularised coordinates through a linearized model. This provides insight into the motion of the minor asteroid about the main asteroid, allowing strategies to engineer the capture process to be developed. Based on the topology of the zero velocity curves (ZVCs) for the PPRTBP, we determine the capture region for the problem by developing initial condition maps (ICMs) and investigate the details of the dynamical process for capture. Two capture strategies are then proposed to engineer and extend the possibility for capture of the minor asteroid in binary pair. One is a re-phasing manoeuvre before encounter, which guarantees that the particle is within the capture region of the ICMs. The other is an optimal, single-impulse transfer during encounter to ensure transfer through the ZVC bottleneck and capture of the minor asteroid by the planetary body. The purpose of the paper is to explore such engineering strategies, rather than to provide new insights into natural capture dynamics.

Key words

Planar parabolic restricted three-body problem · Binary asteroids · Zero velocity curves · Initial condition maps · Asteroid capture

1 Introduction

Asteroids can provide important information on how the solar system both formed and evolved [1-3]. Thought to be leftover planetesimals, asteroids have a close relation to the processes shaping the formation of the planets in the solar system. Among them, the most primitive asteroids may contain original material from the solar nebula where the solar system formed [4]. Recent studies demonstrate that asteroids may also be able to provide other key clues on the formation of the solar system, which cannot be derived from any other source [5, 6].

[1] PhD Candidate, School of Engineering, University of Glasgow, Glasgow G12 8QQ, UK;
Email : x.liu.3@research.gla.ac.uk

[2] Professor, School of Engineering, University of Glasgow, Glasgow G12 8QQ, UK

[3] Lecturer, School of Engineering, University of Glasgow, Glasgow G12 8QQ, UK

In addition, asteroids could provide a rich pool of resources to support future space industrialization [7-9]. Based on current known terrestrial reserves and growing global consumption, easily accessible key elements for industry could be exhausted within 50-60 years [10]. In response, asteroids could in principle be a potential source of such key resources to support long-term prosperity on Earth and future space exploration ventures.

Moreover, asteroids may pose a long-term threat due to the possibility of impacts on the surface of the Earth, with regional or even global effects [11, 12]. To mitigate such threats, or to assay asteroids for future resource use, it is necessary first to investigate asteroids in-situ. For these reasons, asteroids have drawn the attention of the planetary science community, which has led to an increasing number of asteroid missions, such as Hayabusa 1&2 [13], Deep Impact [14] and Rosetta [15]. Capturing small near Earth asteroids (NEAs) into stable orbits in the vicinity of the Earth is also an effective means of direct investigation. NASA has proposed the Asteroid Redirect Mission (ARM), whose goal is to send a robotic spacecraft to a selected NEA and return a large boulder to a parking orbit around the moon [16].

The artificial capture of asteroids in the vicinity of the Earth is clearly a challenging problem which will require solutions to a range of technical issues. A number of strategies have been proposed to investigate this problem. The simplest method is to transfer the asteroid in a two-body model. For example, Hasnain et al. [17] applied the patched conics method to model the transfer of an asteroid to the vicinity of the Earth. In their work, they identified 23 asteroids (lowest Δv 700 ms^{-1}) which could be captured within 10 years, with the best target being 2007CB27. They also suggested that the velocity increment for capture could be decreased if lunar fly-bys were implemented. The circular restricted three-body problem (CRTBP) can also be used to model the capture problem. To capture NEAs using this model, Baoyin et al. [18] proposed a method to alter the asteroid's energy using an impulsive manoeuvre in the Sun-Earth CRTBP, in which, with the proper Jacobi constant, the asteroid becomes trapped within the zero velocity curves (ZVCs) in the neighbourhood of the Earth. In their work, the best target was 2009BD with lowest Δv approximately 410 ms^{-1}. Similarly, Urrutxua et al. [19] investigated the capture methods through an impulsive Δv and low-thrust manoeuvre. Another method for asteroid capture is to utilize the invariant manifolds or weak stability boundaries (WSBs) associated with periodic orbits around the L_1 and L_2 points [20]. Yárnoz et al. [21] investigated this method and listed 12 target objects, which can be captured with velocity increments less than 500 ms^{-1}, the so-called easily retrievable objects (EROs). The work has also been extended to capture dynamics at the L_1 and L_2 points in the Earth-Moon system [22].

Natural captures are common phenomena for celestial bodies [23, 24]. An understanding of related mechanics can provide significant insights in developing strategies to engineer the capture process. In general, there are a number of classical theories for the primordial natural capture of celestial bodies: gas drag (energy dissipation due to circumplanetary gas) [25] and pull-down (rapid growth of the planetary mass) [26]. Clearly, pull-down is unfeasible for artificial capture. Similar to gas drag capture, an aero-assisted method has been considered [27] to capture asteroids into bound Earth orbits. However, this method is only suitable for small meter-sized asteroids, due to collision risks and the mechanical properties of target asteroids [28, 29]. There also exists a class of *N*-body interactions for capture. Reference [30] provides a detailed review of capture through *N*-body interactions. Astakhov et al. [31] first studied chaos-

assisted capture in the CRTBP and then extended the work to the elliptical restricted three-body problem (ERTBP) [32]. Using chaos-assisted capture, Verrier et al. [33] investigated the artificial capture of asteroids into Earth orbit through the use of Kolmogorov-Arnold-Moser (KAM) tori, which verified that long-term temporary capture is possible. While, due to the impossibility of permanent capture using conservative gravitational interaction alone in the CRTBP [34, 35], chaos-assisted capture should in principle be considered along with an energy-dissipation strategy to achieve permanent capture [30].

In the above studies, target asteroids were treated as single asteroid systems. However, binary asteroids are also known to exist. First observed directly by the Galileo spacecraft in 1993 [36, 37], binary asteroids had been both controversial and neglected [38, 39]. However, in the last two decades, several hundred binary asteroids have been discovered. Based on the work of Bottle and Melosh [40], the fraction of binary pairs is estimated at approximately 15% of the total NEA population. There have now been some 330 objects identified as binary-asteroid systems or multi-asteroid systems[4]. Given this relative abundance of binary asteroids, it is of interest to investigate strategies to engineer the capture of one member of a binary asteroid pair during the flyby of a planetary body.

Few publications addressed the topic of binary asteroid capture until the work of Agnor. Agnor et al. [23] firstly considered a binary-asteroid capture model for the origin of Neptune's satellite Trion which successfully overcame the limitations of classical capture theories. Afterwards, Philpotta et al. [30] extended this idea to Jupiter's irregular satellites. Gaspar et al. [41, 42] adopted the model in the Sun-Jupiter CRTBP with their numerical results agreeing well with observational data. Borum et al. [43] studied the capture of binary asteroids at the Earth through a Monte Carlo method. Gong et al. [29] also considered the Sun's perturbation on a binary capture at the Earth. In related work, Sari et al. [44] introduced a binary-star model for the origin of hyper-velocity stars, which can provide insights into the asteroid capture problem. Since binary capture is in general a multi-body problem, it is difficult to derive analytical results without gross simplification [23]. For this reason, prior work has mainly focused on numerical simulation of general multi-body problems to provide a qualitative analysis through statistical results [23, 30, 41-43, 45]. Some authors adopt strict constrains (such as an impulse approximation with instantaneous binary disruption) for simplification. However, the approximate analytical results can deviate far from numerical results. Few studies can therefore provide an overarching theoretical analysis for binary capture mechanics.

In this paper, we will investigate the feasibility of capturing the minor asteroid of a binary pair through disruption of the binary system during a close encounter with a generic central body. Leveraging the gravitational binding energy between the binary asteroid pair, this method achieves a route towards the artificial capture of the minor asteroid of the binary asteroid pair at the central body. As an initial engineering model of the problem, we adopt the planar parabolic restricted three-body problem (PPRTBP) approximation to provide a simple and clear description of the dynamics of binary capture. The dynamical equations for the problem are firstly obtained and then the associated sets of regularised equations are derived. An approximate analytical solution for motion in the vicinity of the main asteroid in the regularised

[4] Data available online at http://www.johnstonsarchive.net/astro/asteroidmoons.html [retrieved April 2018]

system is also provided through a linearized model. Generally, three types of final evolution for the minor asteroid are defined as, capture by central body, bound with the main asteroid and escape. Then, based on the topology of the ZVCs of the PPRTBP, we determine capture regions by developing initial condition maps (ICMs), and then investigate the dynamical process for capture in some detail. The model is then used to provide an initial assessment of strategies to artificially engineer the capture process. Again, the purpose of the paper is to explore such engineering strategies, rather than to provide new insights into natural capture dynamics.

Two strategies are then proposed to extend the possibility of engineering the capture of the minor asteroid of a binary pair; a re-phasing manoeuvre before encounter to engineer the location of the asteroid in the ICM and a single-impulse transfer during encounter to ensure transfer through the ZVC bottleneck. Although in general a large main asteroid is required to enable such capture process, with a radius typically larger than 40 km for permanent capture within Earth's Hill sphere (to provide sufficient gravitational binding energy which can be exchanged), this paper investigates the underlying dynamics of the problem required to engineer the capture process in a non-dimensional manner. This can provide new insights for capture around other planets and their satellites (such as the Moon and Mars).

The paper is organized as follows. Section 2 provides a brief description of the PPRTBP, Section 3 derives the regularised equations of the PPRTBP to avoid singularities. In Section 4, a linear analysis is provided for analytical insights into the capture problem. In Section 5, ICMs are then illustrated and strategies for capture are presented in Section 6, while, conclusions are drawn in Section 7.

2 The Planar Parabolic Restricted Three-Body Problem

2.1 Equations of motion

Consider a scenario with three mutually interacting bodies in an inertial frame of reference. Two of the primaries P_1 and P_2, of mass m_1 and m_2 respectively, move in a parabolic orbit around their barycentre. The third body P_3, a massless particle, moves under the gravitational field generated by the primaries and orbits in the same plane as the primaries, without perturbing them. The problem described above is the planar parabolic restricted three-body problem (PPRTBP) [46-49, 52]. Considering a binary asteroid pair approaching a central body, we can approximate the dynamics of the problem through PPRTBP, denoting the central body as P_1, the main asteroid as P_2 and the minor asteroid as P_3, as shown in Fig. 1. In this approximation, the minor asteroid is assumed to be massless and so the mass of the binary system is comprised of the main asteroid.

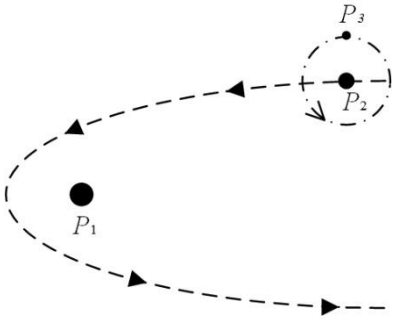

Figure 1. Schematic of the planar parabolic restricted three-body problem.

The mass ratio of system is defined as $\mu = m_2/(m_1 + m_2)$ and, in the barycentre-centred inertial frame OX_IY_I, shown in Fig.2, the dynamical equations for the massless particle's coordinates $\mathbf{R}_3 = (X_I, Y_I)$ are given by

$$\begin{aligned} \ddot{X}_I &= \frac{\partial W}{\partial X_I} \\ \ddot{Y}_I &= \frac{\partial W}{\partial Y_I} \end{aligned} \tag{1}$$

where $\dot{} = \frac{d}{dt}$ is the derivative with respect to time t and the gravitational potential W is defined by

$$W = \frac{Gm_1}{|\mathbf{R}_1|} + \frac{Gm_2}{|\mathbf{R}_2|}$$

where G is the gravitational constant and $\mathbf{R}_1$, $\mathbf{R}_2$ are the position vectors of P_3 with respect to P_1 and P_2 in the barycentre-centred inertial frame OX_IY_I, again shown in Fig. 2.

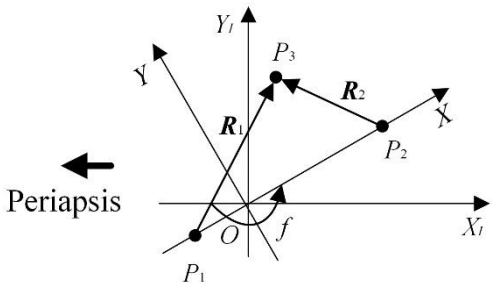

Figure 2. PPRTBP in frame OX_IY_I and frame OXY.

Equation (1) can also be transformed to a non-uniformly rotating frame OXY, in which the origin is the system's barycentre and the X axis always points from P_1 to P_2. The relationship between the frame OX_IY_I and the frame OXY is also shown in Fig. 2. The true anomaly f is defined as the angle between the direction of periapsis and the current position of P_2, whose sign obeys the right-hand rule.

As the frame OXY rotates relative to the inertial frame of reference, as P_2 moves along a parabolic orbit relative to P_1, the dynamical equations for the coordinates of P_3, $\mathbf{R}_3 = (X, Y)$, can be written in the rotating frame OXY as the following system (see [46], for details)

$$\begin{aligned} \ddot{X} - 2\dot{f}\dot{Y} - \dot{f}^2 X - \ddot{f}Y &= \frac{\partial W}{\partial X} \\ \ddot{Y} + 2\dot{f}\dot{X} - \dot{f}^2 Y + \ddot{f}X &= \frac{\partial W}{\partial Y} \end{aligned} \tag{2}$$

Assuming that the distance P_1-P_2 is unitary, we introduce a non-uniformly rotating pulsating frame Oxy, in which the position of P_3 is defined by new non-dimensional variables $\mathbf{r} = (x, y)$ as

$$(x, y) = \frac{(X,Y)}{|\mathbf{R}_1 - \mathbf{R}_2|}$$

and so the primaries remain fixed along the *x*-axis at $(-\mu, 0)$ and $(1-\mu, 0)$ respectively, as shown in Fig. 3.

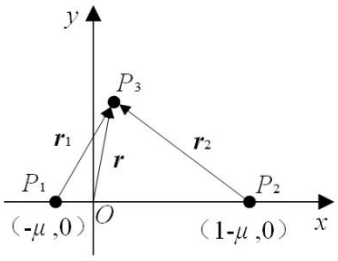

Figure 3. PPRTBP in synodic pulsating frame Oxy.

Now, instead of choosing the true anomaly f as a new independent variable, we reparametrize time t as

$$\frac{dt}{ds} = \sqrt{\frac{2|\mathbf{R}_1-\mathbf{R}_2|^3}{G(m_1+m_2)}} \tag{3}$$

Following Reference [45-47], substituting the new non-dimensional variables (x, y) and the new independent variable s into Eq. (2), we can derive the dynamical equation of P_3 in the rotating-pulsating frame Oxy, defined by

$$x'' + \sin\theta x' - 4\cos\theta y' = \frac{\partial\Omega}{\partial x} \tag{4a}$$

$$y'' + \sin\theta y' + 4\cos\theta x' = \frac{\partial\Omega}{\partial y} \tag{4b}$$

$$\theta' = \cos\theta \tag{4c}$$

where $' = \frac{d}{ds}$ is the derivative with respect to s and the potential function of the PPRTBP, Ω, is now given by

$$\Omega = \frac{2(1-\mu)}{r_1} + \frac{2\mu}{r_2} + (1-\mu)r_1^2 + \mu r_2^2 \tag{5}$$

Note that $\theta = f/2$ is a new auxiliary variable introduced to represent the relative position of the two primaries along the parabolic orbit. The distances in Eq. (5) are given by $r_1 = \sqrt{(x+\mu)^2 + y^2}$, $r_2 = \sqrt{(x+\mu-1)^2 + y^2}$.

2.2 Equilibrium points and homothetic solutions

In order to proceed, the equilibrium points of Eq. (4) can be found and are given by

$$\begin{gathered} \theta = \pm\frac{\pi}{2} \\ \nabla\Omega = 0 \\ x' = 0 \\ y' = 0 \end{gathered} \tag{6}$$

which are similar to the equilibrium points of the CRTBP. We denote the equilibrium points by L_i^- and L_i^+ $(i = 1, \cdots, 5)$ for $\theta = -\pi/2$ and $\theta = \pi/2$, respectively. Since $\theta = f/2$, $\theta =$

$\pm\pi/2$ can also be represented as $f = \pm\pi$, which means that physically P_2 is at infinity with respect to P_1. To connect the equilibrium points L_i^- and L_i^+, a set of homothetic solutions can be derived as the following system (see [46], for details)

$$\begin{aligned} \nabla\Omega &= 0 \\ x' &= 0 \\ y' &= 0 \\ \theta &= \sin^{-1}(\tanh s) \end{aligned} \tag{7}$$

where the auxiliary variable θ is obtained by direct integration of Eq. (4c) and the homothetic solutions are denoted by HS_i $(i = 1, \cdots, 5)$. Clearly, these five homothetic solutions are homographic, i.e. they maintain the same (collinear or triangular) configuration with respect to the primaries, as shown in Fig. 4. Physically, the homothetic solutions exist in the rotating frame, with their location pulsating as P_2 moves along its parabolic orbit relative to P_1.

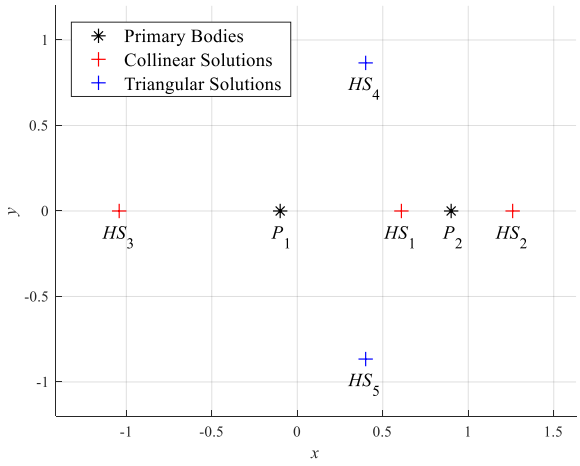

Figure 4. Homothetic solutions in frame Oxy with μ=0.1.

2.3 Jacobi function and Hill's region for allowed motion

Furthermore, analogous to the Jacobi constant in the CRTBP, from Eq. (4) we can derive a similar relationship in the PPRTBP, termed the Jacobi function, defined by

$$C(x, y, x', y') = 2\Omega - \left(x'^2 + y'^2\right) \tag{8}$$

The Jacobi function C is not constant along solutions since

$$C' = 2\left(x'^2 + y'^2\right)\sin\theta \tag{9}$$

Moreover, since its derivative depends explicitly on θ, the Jacobi function C has a piecewise-like behaviour along the solutions of the dynamical equations (except the homothetic solutions, whose Jacobi functions are constant). More precisely, when $\theta \in [0, \pi/2]$ the Jacobi function increases, whereas when $\theta \in [-\pi/2, 0]$ the Jacobi function decreases, and so it has a gradient-like property.

For a given Jacobi function value c, Eq. (8) defines an energy surface $\mathcal{C}$ as [48]

$$\mathcal{C}(\mu, c) = \{(x, y, x', y') | C(x, y, x', y') = c\} \tag{10}$$

The projection of $\mathcal{C}(\mu, c)$ onto the *x*-*y* plane is the so-called Hill's region, which determines the allowed region for motion in configuration space, defined as

$$\mathcal{H}(\mu, c) = \{(x, y) | 2\Omega \geq c\} \tag{11}$$

We can also define the zero-velocity curve (ZVC), the boundary of Hill's region as

$$\mathcal{Z}(\mu, c) = \{(x, y) | 2\Omega = c\} \tag{12}$$

As the underlying topology of the ZVC in the PPRTBP is the same as the CRTBP, we can adopt the ZVC as the criterion to determine the necessary condition for binary disruption.

Denoting the values of the Jacobi function for the homothetic solutions by C_i $(i = 1, \cdots, 5)$ respectively, Fig. 5 shows the topology of the ZVC and the possibility of disruption of the binary pair when the ZVC at P_1 and P_2 connects. As the Jacobi function varies with time, the ZVC also evolves with time. Therefore when C reaches critical values (such as the values of the collinear homothetic solutions), the bottlenecks around them open or close. Then the minor asteroid P_3 may transfer to different regions of motion, for example from an orbit about the main asteroid P_2 to an orbit about the central body P_1. The ZVC can therefore be used to provide an interpretation of the conditions required for disruption of the binary asteroid in the PPRTBP.

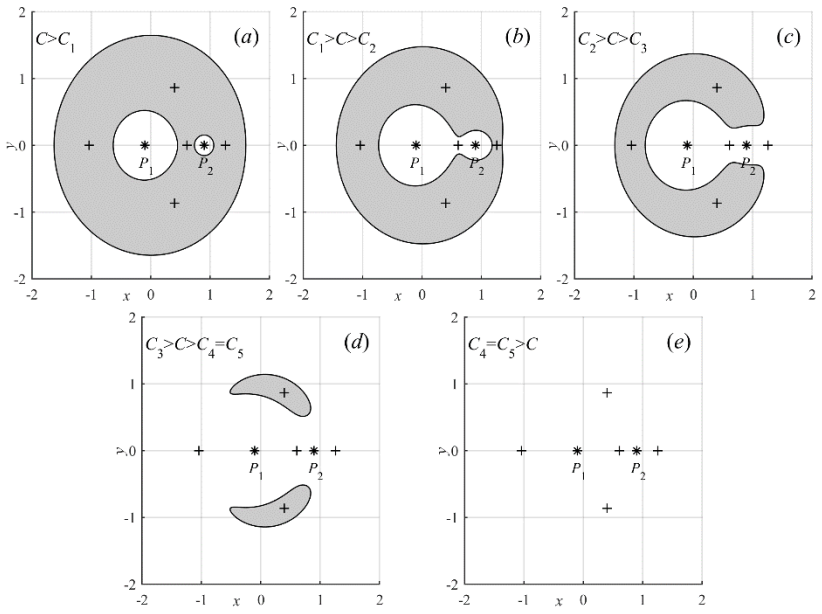

Figure 5. Realms of possible motion in frame Oxy with μ=0.1.

3 Regularised Equations

In computing the trajectory of P_3, collisions with either P_1 or P_2 may occur. In such cases, a singularity will arise in the numerical integration of Eq. (4), due to the inverse square nature of gravity, which will cause the integrator to reduce the integration step-size at a prohibitive cost or even to fail. Therefore, to eliminate singularities and improve the efficiency of numerical integration, it is necessary to derive a set of regularised equations from Eq. (4). As we only

consider the planar case, the Levi-Civita method is sufficient [50]. Since it is a local regularisation method, we firstly move the origin of the coordinate system from the barycentre to the primary body where the singularity will be removed. Then, introducing a new transformation as

$$x + iy = (w_1 + iw_2)^2$$

the configuration space (x, y) maps to the complex plane $\mathbf{w} = (w_1, w_2)$, where $i^2 = -1$. For regularisation, we also introduce a new independent variable transformation as [50]

$$\frac{ds}{d\tau} = 4(w_1^2 + w_2^2) \tag{13}$$

where τ is the new time-like variable. Substituting the new transformations for the position variables and time into Eq. (4), we can derive the related regularised equations. For the case of regularisation in a neighbourhood of P_1, which is a set of points within a circle of radius r_{LC} with respect to P_1, the regularised equations of motion are found to be

$$\begin{gathered}
\frac{d^2w_1}{d\tau^2} + 4r_1\left(\sin\theta\frac{dw_1}{d\tau} - 4\cos\theta\frac{dw_2}{d\tau}\right) = 2w_1(A_1 - 2C) \\
\frac{d^2w_2}{d\tau^2} + 4r_1\left(\sin\theta\frac{dw_2}{d\tau} + 4\cos\theta\frac{dw_1}{d\tau}\right) = 2w_2(A_2 - 2C) \\
\frac{dC}{d\tau} = 2\left[\left(\frac{dw_1}{d\tau}\right)^2 + \left(\frac{dw_2}{d\tau}\right)^2\right]\sin\theta \\
\frac{d\theta}{d\tau} = 4r_1\cos\theta \\
\frac{ds}{d\tau} = 4r_1
\end{gathered} \tag{14}$$

with $r_1 = w_1^2 + w_2^2$, $r_2 = \sqrt{(w_1^2 + w_2^2)^2 - 2(w_1^2 - w_2^2) + 1}$ and

$$\begin{aligned}
A_1 &= 8\mu(-w_1^2 + 3w_2^2 + 1)/r_2^3 + 12r_1^2 + 4\mu(1 - 4w_1^2) \\
A_2 &= 8\mu(-3w_2^2 + w_2^2 + 1)/r_2^3 + 12r_1^2 + 4\mu(1 + 4w_2^2)
\end{aligned}$$

Similarly, we can derive the regularised equations in a neighbourhood of P_2, which yields

$$\begin{gathered}
\frac{d^2w_1}{d\tau^2} + 4r_2\left(\sin\theta\frac{dw_1}{d\tau} - 4\cos\theta\frac{dw_2}{d\tau}\right) = 2w_1(A_3 - 2C) \\
\frac{d^2w_2}{d\tau^2} + 4r_2\left(\sin\theta\frac{dw_2}{d\tau} + 4\cos\theta\frac{dw_1}{d\tau}\right) = 2w_2(A_4 - 2C) \\
\frac{dC}{d\tau} = 2\left[\left(\frac{dw_1}{d\tau}\right)^2 + \left(\frac{dw_2}{d\tau}\right)^2\right]\sin\theta \\
\frac{d\theta}{d\tau} = 4r_2\cos\theta \\
\frac{ds}{d\tau} = 4r_2
\end{gathered} \tag{15}$$

with $r_2 = w_1^2 + w_2^2$, $r_1 = \sqrt{(w_1^2 + w_2^2)^2 - 2(w_1^2 - w_2^2) + 1}$ and

$$\begin{aligned}
A_3 &= 8(1-\mu)(w_1^2 - 3w_2^2 + 1)/r_1^3 + 12r_2^2 + 4(1-\mu)(1 + 4w_1^2) \\
A_4 &= 8(1-\mu)(3w_1^2 - w_2^2 + 1)/r_1^3 + 12r_2^2 + 4(1-\mu)(1 - 4w_1^2)
\end{aligned}$$

In practice, when r_1 or r_2 are below a critical value r_{LC}, Eq. (14) or Eq. (15) are used. Similarly, when r_1 and r_2 are greater than r_{LC}, Eq. (4) is adopted. In this paper, we choose $r_{LC} = 0.02$ in non-dimensional units, empirically.

4 Linear Analysis for Motion around P_2

Based on the previous sections, it can be seen that by adopting a suitable variable transformation, the PPRTBP has similar expressions and properties to the CRTBP, while the PPRTBP is much more complex than the CRTBP due to its time-varying coefficients and aperiodic nature [45-47]. In the CRTBP, (quasi) periodic orbits around equilibrium points and the related invariant manifolds provide the key insights for the dynamical structure of the system [20, 51]. Arguably, these methods may need some new developments to provide the same insights into the PPRTBP, given its complexity. Some work on this issue has been done in References [47-48], while the complete description of the dynamical structure of the PPRTBP is still an open problem, which is out of the scope of the current paper. For this reason, in this section, we perform a linear analysis for the motion of the particle P_3 in the vicinity of the main asteroid P_2 in the regularised coordinate system. In spite of its simplicity, the analysis provides useful insights into the problem, including the necessary conditions required for capture.

As the ZVC topology evolves with time, a disruption of the binary pair may occur during the close encounter with the central body. The ZVC topology therefore offers a useful condition to determine if disruption of the binary pair may occur and can provide further insights into the motion of the particle P_3, as will be seen later. First though, due to the complex nature of the PPRTBP, the model will now be simplified to obtain analytical insights into the problem. As the particle P_3 orbits about P_2 initially, we adopt the regularised equations of motion Eq. (15) to eliminate the singularity around the main asteroid P_2.

Then, we assume w_1 and w_2 satisfy $\|\mathbf{w}\| \ll 1$, with order of magnitude $\mathcal{O}(\mathbf{w})$. In the following analysis at Eq. (27), we can also show that $(dw_1/d\tau)^2 + (dw_2/d\tau)^2 \sim \mathcal{O}(\mu)$, with $\mu \ll 1$. Then Eq. (15) can be expanded through the use of a Taylor series, neglecting the second and higher order terms of $\mathbf{w}$ to obtain a linearized model as

$$\begin{aligned} \frac{d^2w_1}{d\tau^2} &= 4w_1[6(1-\mu) - C] \\ \frac{d^2w_2}{d\tau^2} &= 4w_2[6(1-\mu) - C] \\ \frac{dC}{d\tau} &= 0 \\ \frac{d\theta}{d\tau} &= 0 \\ \frac{ds}{d\tau} &= 0 \end{aligned} \tag{16}$$

This can be interpreted by representing the system as a hierarchy of two different time and length scales, one for the relative motion within the P_2-P_3 binary system and one for the parabolic orbit of P_2 with respect to P_1. Clearly, the former has a much faster time-scale and a much smaller length-scale than the later. Therefore, when we investigate the relative motion within the binary system, we can assume that the motion along the parabolic orbit is frozen. In this linear model, the parameters referring to parabolic motion (such as θ, s and C) can

therefore be treated as constant, and their derivatives are zero, as is clear from the linearization in Eq. (16).

Using the linear model, we can obtain analytical solutions to Eq. (16) directly, the properties of which will depend on the value of C. It can be seen that if $C < 6(1-\mu)$, the analytical solutions are simply

$$\begin{aligned} w_1 &= a_1 e^{\lambda\tau} + a_2 e^{-\lambda\tau} \\ w_2 &= a_3 e^{\lambda\tau} + a_4 e^{-\lambda\tau} \\ \lambda &= 2\sqrt{6(1-\mu) - C} \end{aligned} \tag{17}$$

for constants a_i $(i = 1, \cdots, 4)$ which are exponentially divergent, while if $C = 6(1-\mu)$, the solutions are

$$\begin{aligned} w_1 &= a_1\tau + a_2 \\ w_2 &= a_3\tau + a_4 \end{aligned} \tag{18}$$

which are polynomially divergent. Finally, if $C > 6(1-\mu)$, the analytical solutions are

$$\begin{aligned} w_1 &= a_1 \cos\lambda\tau + a_2 \sin\lambda\tau \\ w_2 &= a_3 \cos\lambda\tau + a_4 \sin\lambda\tau \\ \lambda &= 2\sqrt{C - 6(1-\mu)} \end{aligned} \tag{19}$$

which are bounded and periodic.

The critical value of C obtained above can also be verified from the energy in a two-body model. In previous studies [23, 41, 42], the two-body energy E between P_2 and P_3 is always adopted as a key index for the disruption in binary asteroid pairs. Following this, the relative velocity of P_3 with respect to P_2 can be expressed in the inertial frame OX_IY_I as

$$\mathbf{V}_{r2\_IN} = nq\cos\theta \begin{bmatrix} -\cos 2\theta & \sin 2\theta \\ -\sin 2\theta & -\cos 2\theta \end{bmatrix} \begin{bmatrix} \frac{dx}{ds} \\ \frac{dy}{ds} \end{bmatrix} + 2nq\cos\theta \begin{bmatrix} \sin\theta & \cos\theta \\ -\cos\theta & \sin\theta \end{bmatrix} \begin{bmatrix} x-1+\mu \\ y \end{bmatrix} \tag{20}$$

with $nq\cos\theta = \sqrt{\frac{G(m_1+m_2)}{2|\mathbf{R}_1-\mathbf{R}_2|}}$, where n and q are the mean motion and the perigee radius of the parabolic orbit of the problem. Then, the two-body energy E_{rlt} between binary pair can be given as

$$E_{rlt} = \frac{\mathbf{V}_{r2\_IN}{}^2}{2} - \frac{Gm_2}{|\mathbf{R}_1-\mathbf{R}_2|r_2} \tag{21}$$

with r_2 is the non-dimensional distance between P_2 and P_3 in the PPRTBP. Substituting Eq. (20) into Eq. (21), after some manipulation yields

$$\left\| \begin{bmatrix} \frac{dx}{ds} \\ \frac{dy}{ds} \end{bmatrix} + 2 \begin{bmatrix} \sin\theta & \cos\theta \\ -\cos\theta & \sin\theta \end{bmatrix} \begin{bmatrix} x-1+\mu \\ y \end{bmatrix} \right\|^2 = \frac{4\mu}{r_2} + 2\bar{E}_{nd} \tag{22}$$

in which, the non-dimensional two-body energy $\bar{E}_{nd}$ is given as

$$\bar{E}_{nd} = \frac{2|\mathbf{R}_1-\mathbf{R}_2|}{G(M_1+M_2)} E_{rlt} \tag{23}$$

As we assume $|r_2| \ll 1$, Eq. (22) can be simplified as

$$\left[\left(\frac{dx}{ds}\right)^2 + \left(\frac{dy}{ds}\right)^2\right] + O(r_2) = \left\| \begin{bmatrix} \frac{dx}{ds} \\ \frac{dy}{ds} \end{bmatrix} + 2 \begin{bmatrix} \sin\theta & \cos\theta \\ -\cos\theta & \sin\theta \end{bmatrix} \begin{bmatrix} x - 1 + \mu \\ y \end{bmatrix} \right\|^2 = \frac{4\mu}{r_2} + 2\bar{E}_{nd} \quad (24)$$

In the PPRTBP, the Jacobi function C is then defined from Eq. (8) as

$$C = \frac{4(1-\mu)}{r_1} + \frac{4\mu}{r_2} + 2(1-\mu)r_1^2 + 2\mu r_2^2 - \left[\left(\frac{dx}{ds}\right)^2 + \left(\frac{dy}{ds}\right)^2\right]$$

Substituting Eq. (24) into Eq. (8), it can also be seen that

$$C = \frac{4(1-\mu)}{r_1} + 2(1-\mu)r_1^2 - 2\bar{E}_{nd} + O(r_2) \quad (25)$$

Then, introducing the regularised variable $\mathbf{w}$ around P_2 and expanding Eq. (25) in a Taylor series yields

$$C = 6(1-\mu) - 2\bar{E}_{nd} + O(\|\mathbf{w}\|^2) \quad (26)$$

Neglecting the second and higher order terms in Eq. (26), the Jacobi function can be expressed as

$$C = 6(1-\mu) - 2\bar{E}_{nd}$$

which reveals the relationship between Jacobi function C and the two-body energy $\bar{E}_{nd}$ (non-dimensional) and E_{rlt} in the linear model. An approximation for the quadratic term can be also derived from Eq. (24), as

$$\left(\frac{dx}{ds}\right)^2 + \left(\frac{dy}{ds}\right)^2 \approx \frac{4\mu}{r_2} + 2\bar{E}_{nd} \sim O\left(\frac{\mu}{r_2}\right)$$

Substituting the regularized variables into the above equation, and after some straightforward simplification, we can derive

$$\left(\frac{dw_1}{d\tau}\right)^2 + \left(\frac{dw_2}{d\tau}\right)^2 \approx 4r_2\left(\frac{4\mu}{r_2} + 2\bar{E}_{nd}\right) \sim O(\mu) \quad (27)$$

which has been applied earlier in the derivation of Eq. (16).

Clearly, C has a critical value of $6(1-\mu)$ which is equivalent to $\bar{E}_{nd} = 0$ and $E_{rlt} = 0$. When $C > 6(1-\mu)$, the two-body energy $E_{rlt} < 0$ and the motion of P_3 around P_2 is bound and (quasi) periodic, otherwise the two-body energy $E_{rlt} \geq 0$ and the motion is unstable and divergent. Therefore, using the linear analysis of the regularised equations of motion, a useful necessary condition for disruption of the binary pair can therefore be determined. This linear analysis will also be verified through numerical simulations in Section 5 and will be useful in engineering artificial capture.

5 Numerical Simulation

Similar to [52], we now assume, in the inertial frame, that the particle P_3 moves along an initial circular orbit with respect to the main asteroid P_2. The initial positions of P_3 for

simulation are then defined by a non-uniform grid, which is finer close to P_2 and coarser in the rest of the domain, using

$$\begin{gathered} x = 1 - \mu + r_2 \cos(\alpha - \beta) \\ y = r_2 \sin(\alpha - \beta) \\ r_2 = kR_{sec} \\ k = \begin{cases} 1.1, 1.2, 1.3 \cdots, 14.9, 15 & 1.1 \le k \le 15 \\ 16, 17, \cdots, 999, 1000 & 16 \le k \le 1000 \end{cases} \\ \alpha = 0^{\circ}, 1^{\circ}, 2^{\circ}, \cdots, 358^{\circ}, 359^{\circ} \end{gathered} \tag{28}$$

where R_{sec} is the physical radius of the main asteroid P_2, the angle α is chosen with respect to the inertial frame and β is the initial angle between the inertial frame OX_IY_I and synodic pulsating frame Oxy, as shown in Fig. 6. For the initial velocity, we transform the relative velocity of P_3 with respect to P_2 from the inertial frame to the pulsating frame using Eq. (20), yielding

$$\begin{bmatrix} \frac{dx}{ds} \\ \frac{dy}{ds} \end{bmatrix} + 2 \begin{bmatrix} \sin\theta & -\cos\theta \\ \cos\theta & \sin\theta \end{bmatrix} \begin{bmatrix} x - 1 + \mu \\ y \end{bmatrix} = \frac{1}{nq\cos\theta} \left| \mathbf{V}_{r2\_IN} \right|_{xy}$$

with $|\mathbf{V}|_{xy}$ the projection of the vector $\mathbf{V}$ in the pulsating frame Oxy. As we assume the relative orbit of the binary pair is initially circular, the above expression can be simplified as

$$\begin{bmatrix} \frac{dx}{ds} \\ \frac{dy}{ds} \end{bmatrix} = dir \times \sqrt{\frac{2\mu}{r_2}} \begin{bmatrix} -\sin(\alpha - \beta) \\ -\cos(\alpha - \beta) \end{bmatrix} - 2 \begin{bmatrix} \sin\theta & -\cos\theta \\ \cos\theta & \sin\theta \end{bmatrix} \begin{bmatrix} x - 1 + \mu \\ y \end{bmatrix}$$

in which dir denotes the direction of motion of P_3 with respect to P_2, so that $dir = 1$ for the prograde case (anticlockwise in the planar model) and $dir = -1$ for the retrograde case (clockwise). Both of these two cases will be investigated in this section. These sets of initial conditions will be used later to generate detailed initial condition maps to understand the evolution of the binary pair.

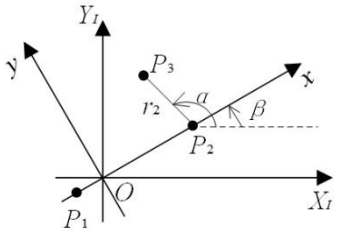

Figure 6. Schematic diagram for initial conditions.

Consider now a specific scenario where a binary asteroid pair is approaching the Earth along a parabolic orbit. If we approximate the dynamics of the problem through the PPRTBP for simplification, then P_1 is the Earth, P_2 is the main asteroid in the binary pair and P_3 is the minor asteroid. Assuming all bodies are ideal spheres and the density of the asteroid is chosen as 2 gcm^{-3} [53], the mass ratio μ will be defined as $\mu_1 = 1.40276 \times 10^{-6}$, $\mu_2 = 1.40276 \times 10^{-9}$ and $\mu_3 = 1.40276 \times 10^{-12}$, corresponding to a main asteroid P_2 with a radius of 100

km, 10 km and 1 km respectively. This broad range of parameters is used for illustration of the specific capture scenario. Other related parameters in the PPRTBP can also be defined. The perigee radius of the parabolic orbit, q, is measured in terms of the radius of P_1 which is denoted as R_{pri}, and varied for different sets of simulation. To ensure the accuracy of the simulation, we locate the binary system on the edge of a fixed disk initially, as References [30, 54] suggest, whose radius is 500 Earth radii, more than twice the radius of the Earth's sphere of influence (SOI).

Besides the initial conditions, the terminal conditions for the simulation also need to be defined. Based on the results of previous investigations [30, 54], one terminal condition is that the simulation will continue until P_2 moves out along its parabolic orbit through the edge of the fixed disk. As discussed earlier, the topology of the ZVC can also be considered as a condition for termination, which is chosen such that the simulation will continue until the bottleneck of the ZVC around HS_1 closes when $\theta \geq 0$.

Normally, when both of these two terminal conditions are satisfied, the simulation will be stopped and then the classification of particle's motion will be judged by the ZVC. Sometimes collisions may occur, so if the relative distance between P_3 and the primaries is less than the physical radius of the primaries, the simulation will also be stopped and a collision recorded. Given the initial conditions of the particle P_3 from the set defined by Eq. (28), the evolution of the binary system can be obtained by integrating the relevant set of regularised or non-regularised equations of motion, using *ode45* with *RelTol* = $3\text{x}10^{-14}$, *AbsTol* = $1\text{x}10^{-14}$ and *MaxStep* = $1\text{x}10^{-3}$ in MATLAB for sufficient numerical integration accuracy.

5.1 Disruption of the binary pair

Except for collision, the final evolution of P_3 can be generally classified by three types, capture, bound and escape. A capture case occurs when the P_2-P_3 binary pair is disrupted and P_3 is captured by P_1 in a bound elliptical orbit. A bound case occurs when the binary system survives after the close encounter with P_1. An escape case occurs when the binary pair is also disrupted, however P_3 escapes from P_1. Similar classification is also defined in References [46-49]. In this section, we provide some examples to illustrate different classifications of motion in the PPRTBP before detailed initial condition maps are generated.

We choose the prograde case and the mass ratio of the problem is defined as $\mu = \mu_1$. With $k = 2.9$, $\alpha = 269^\circ$ and $q = 2$, a capture case is shown in Figs. 7-8. Similarly, a bound case is presented in Figs. 9-10, with $k = 7.2$, $\alpha = 78^\circ$ and $q = 2$. And an escape is also illustrated in Figs. 11-12, with $k = 2.9$, $\alpha = 251^\circ$ and $q = 2$.

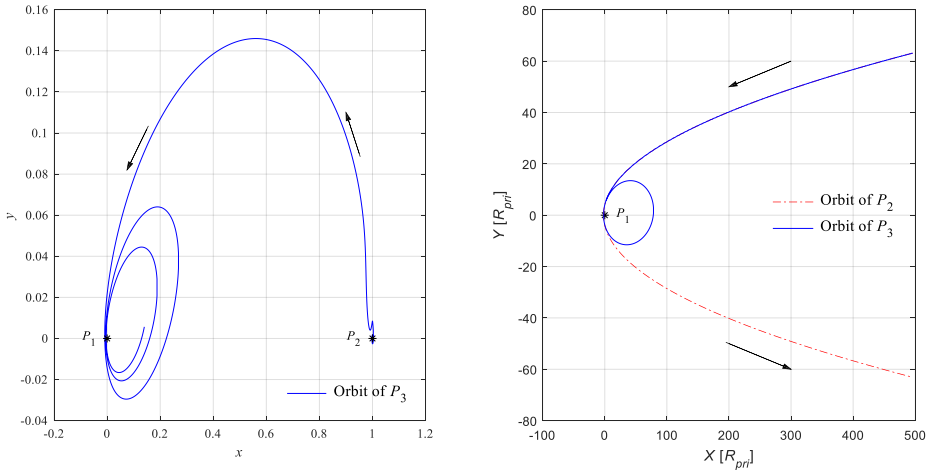

Figure 7. Capture case illustrated. Left: in pulsating frame. Right: in inertial frame.

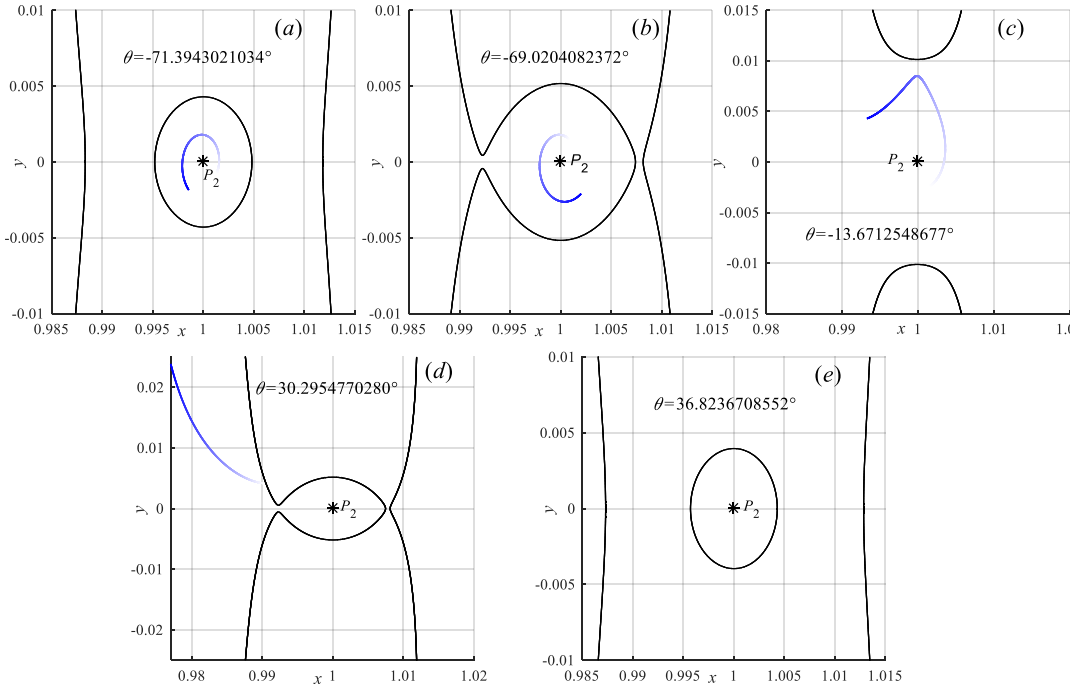

Figure 8. Evolution of ZVC for capture case (zoomed in).
Black and gradient blue correspond to ZVC and trajectory of P_3.

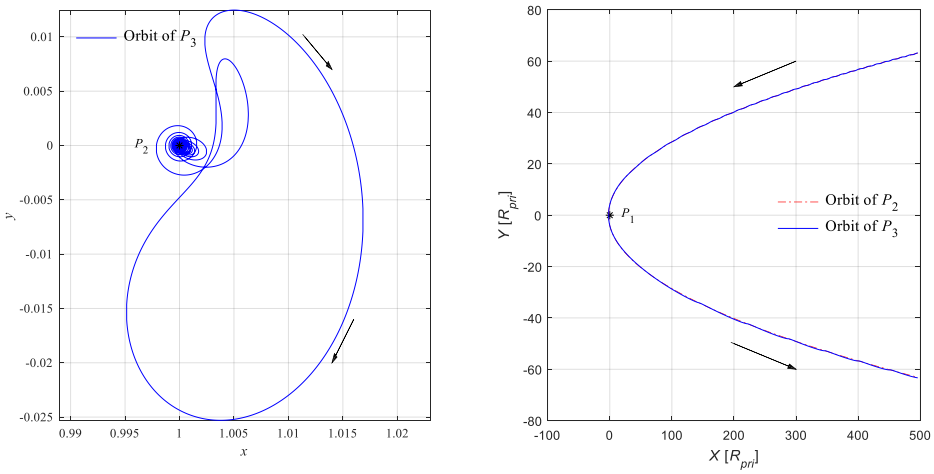

Figure 9. Bound case illustrated. Left: in pulsating frame. Right: in inertial frame.

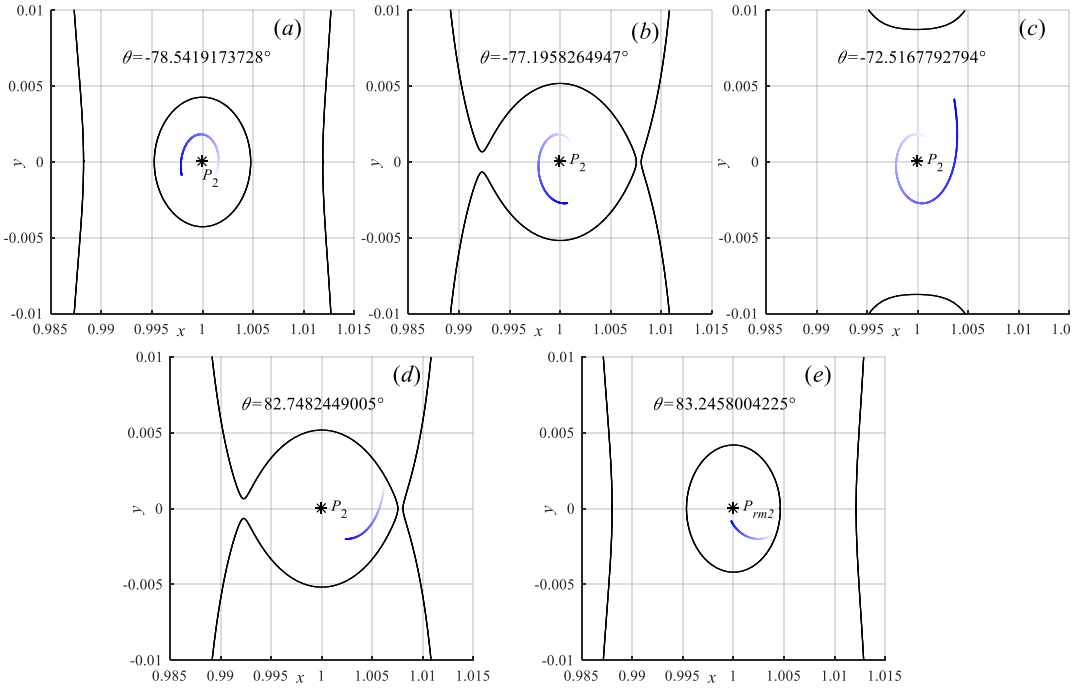

Figure 10. Evolution of ZVC for bound case (zoomed in).
Black and gradient blue correspond to ZVC and trajectory of P_3.

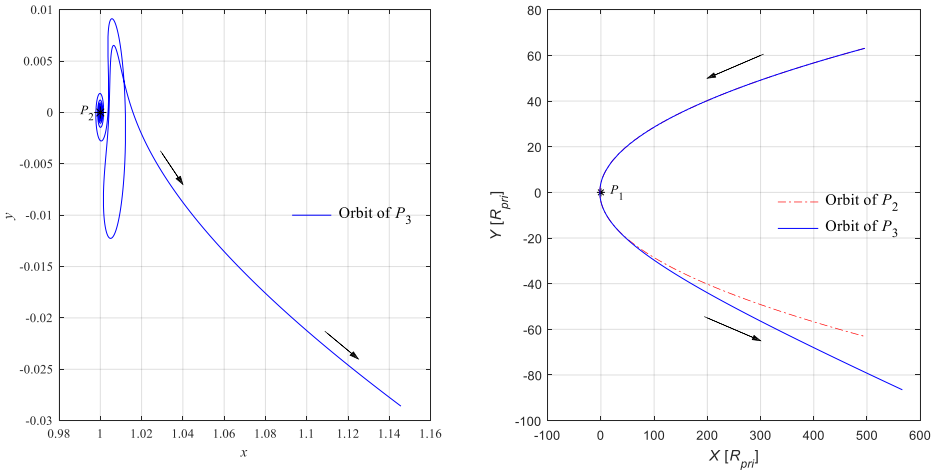

Figure 11. Escape case illustrated. Left: in pulsating frame. Right: in inertial frame.

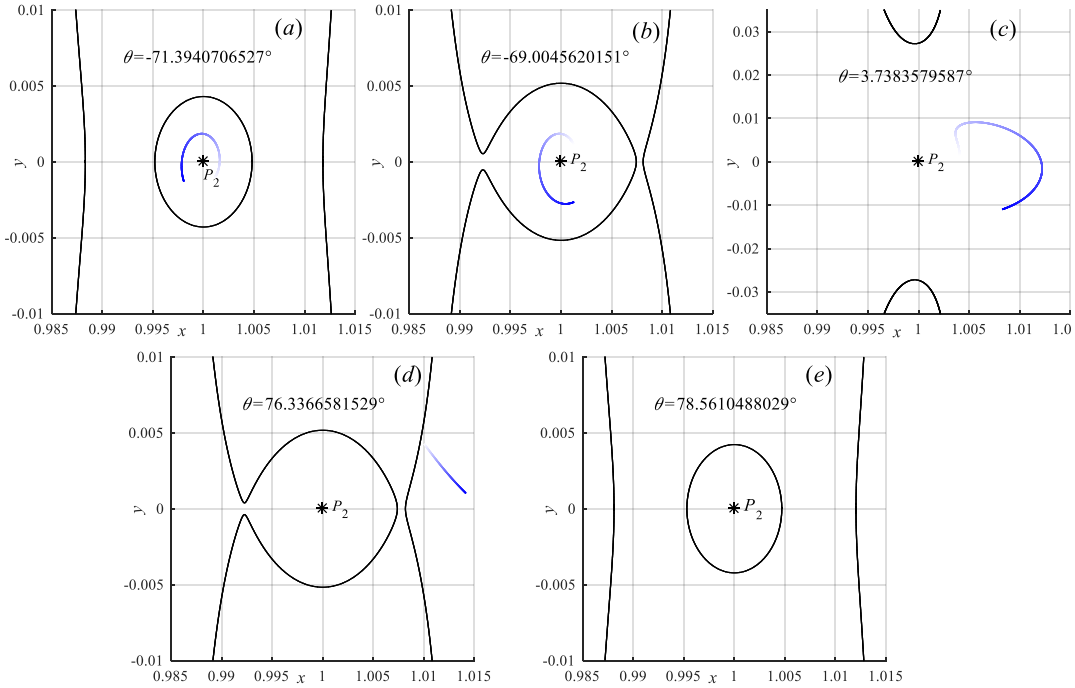

Figure 12. Evolution of ZVC for escape case (zoomed in).
Black and gradient blue correspond to ZVC and trajectory of P_3.

We now take the capture case (Fig. 8) as an example to illustrate the dynamical process during close encounter. In Fig. 8 the ZVC is shown as a solid black line and the trajectory of P_3 is plotted as a solid blue line. At beginning, the bottleneck around HS_1 is still closed and the minor asteroid P_3 is in a bound orbit around the main asteroid P_2, as shown in Fig. 9 (a). With the gradient-like property, the bottleneck of ZVC around HS_1 opens gradually when $\theta < 0$, as shown in Fig. 9 (b), and is at a maximum when $\theta = 0$, while, after that, the bottleneck of ZVC around HS_1 gradually closes when $\theta > 0$. During this process P_3 may pass through the bottleneck around HS_1, in Fig. 9 (c, d) and be permanently captured by the central body P_1

when the bottleneck closes, in Fig. 9 (e). The interpretations of the bound case and the escape case are similar. For conciseness, we will not illustrate them in detail here.

5.2 Regions of capture

In this section the capture region generated for a range of initial conditions of the particle P_3 is considered for different sets of problem parameters, to illustrate their influence on the evolution of the particle. The mass ratio μ is again chosen as $\mu = \mu_1$, $\mu = \mu_2$ and $\mu = \mu_3$. For the perigee radius q, this parameter should be above 1 to avoid a collision between P_1 and P_2. However, a too large value of q will cause insufficient perturbation to disrupt the binary pair. In this paper, we empirically choose the upper limit for q as 20 and, for each mass ratio μ, we vary the perigee radius as $q \in \{2, 5, 10, 15, 20\}$, again in units of the radius of the central body. Given these parameters, we can map the initial conditions in configuration space for the particle based on its subsequent evolution. The initial condition maps (ICMs) for the prograde case, with $\mu = 1.40276 \times 10^{-9}$ and different values of $q = 2$, $q = 10$ and $q = 20$, are shown from Figs. 13-18, to illustrate the effects of q on the final evolution of the binary pair. Similarly, the ICMs, for $q = 20$ and different values of μ, are presented in Figs. 17-22 to reveal the influence of μ. To present the effects of the parameters on the final evolution of the binary pair more concisely, only representative ICMs are shown. Again, the ICM uses the initial condition set of Eq. (28) to illustrate the influence of the initial phasing angle of the binary pair through the angle α and the initial separation through the orbit radius r of P_3 about P_2, shown in units of the radius of P_2.

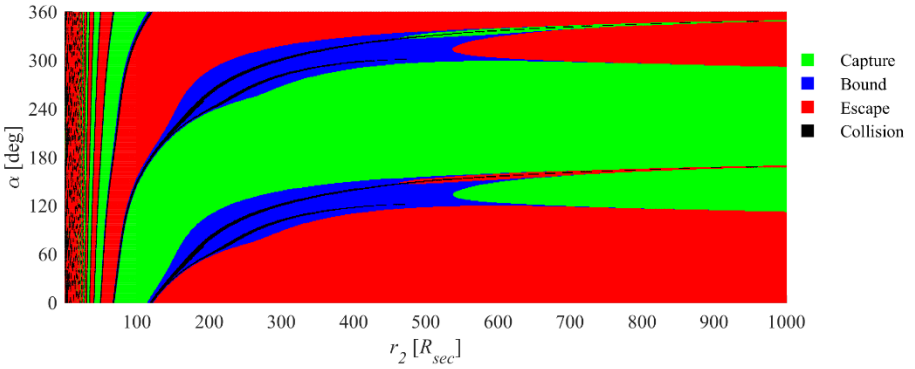

Figure 13. ICM for the prograde case with $\mu = \mu_2$ and q=2.

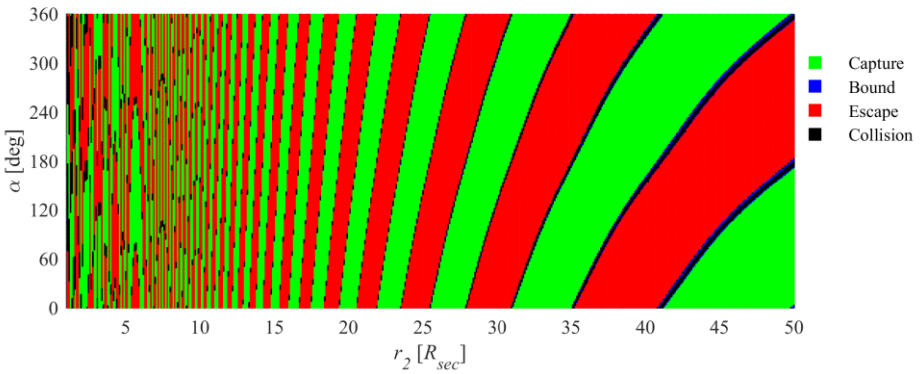

Figure 14. ICM (zoomed in) for the prograde case with $\mu = \mu_2$ and q=2.

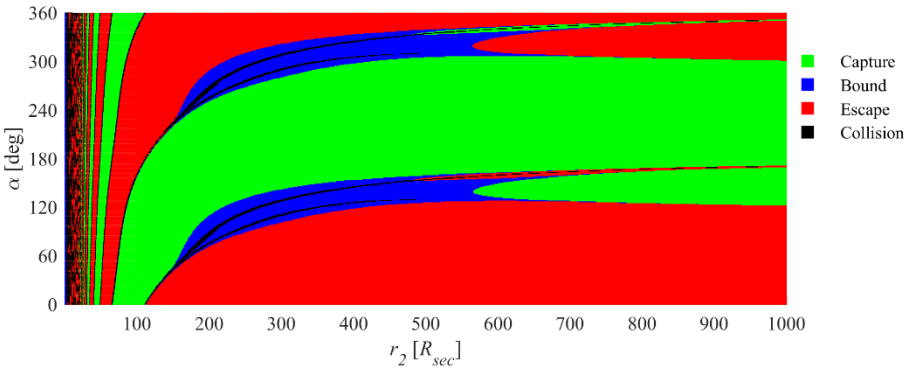

Figure 15. ICM for the prograde case with $\mu = \mu_2$ and q=10.

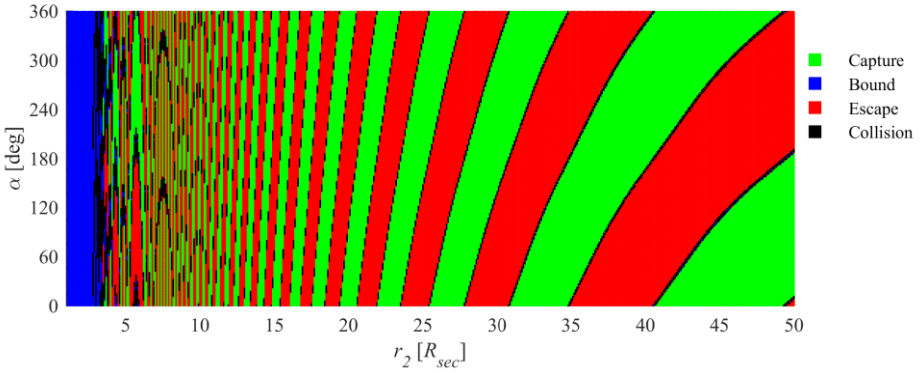

Figure 16. ICM (zoomed in) for the prograde case with $\mu = \mu_2$ and q=10.

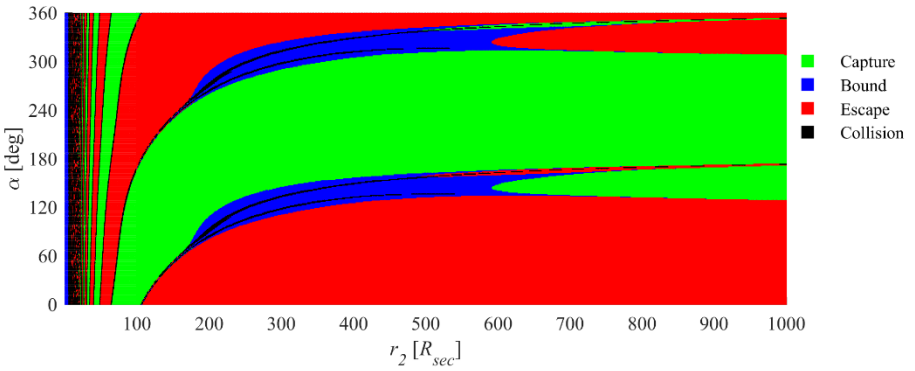

Figure 17. ICM for the prograde case with $\mu = \mu_2$ and q=20.

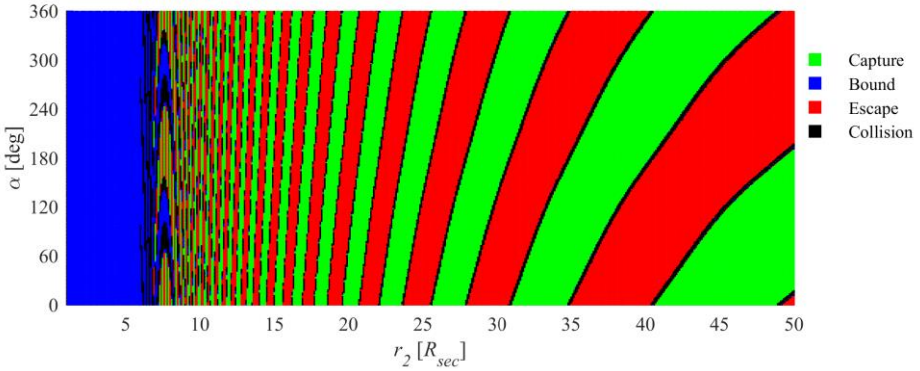

Figure 18. ICM (zoomed in) for the prograde case with $\mu = \mu_2$ and q=20.

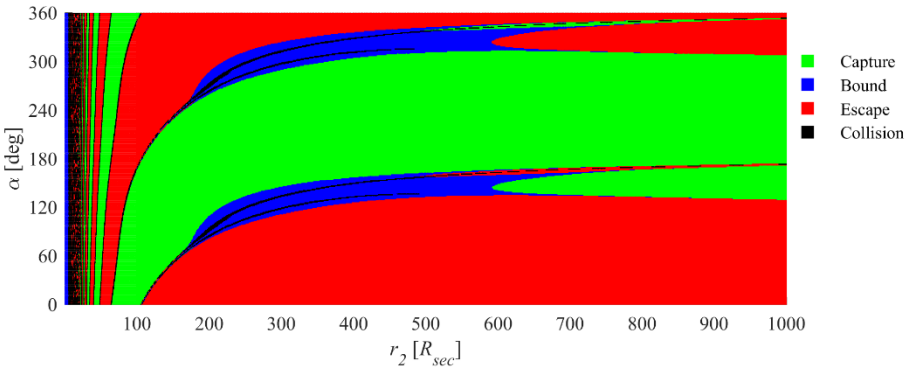

Figure 19. ICM for the prograde case with $\mu = \mu_1$ and q=20.

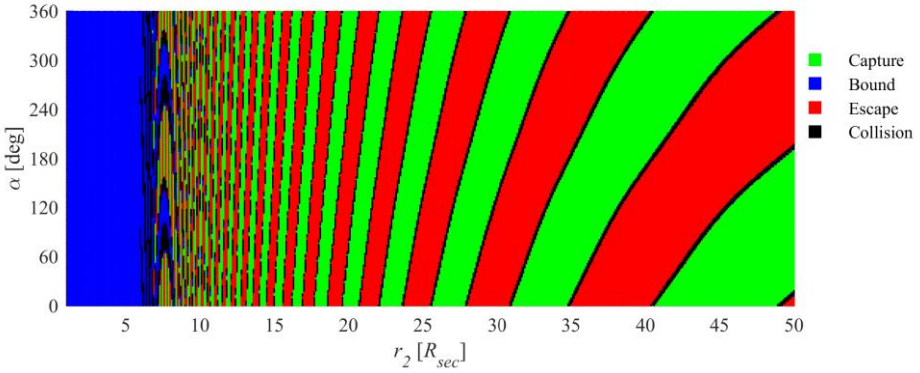

Figure 20. ICM (zoomed in) for the prograde case with $\mu = \mu_1$ and q=20.

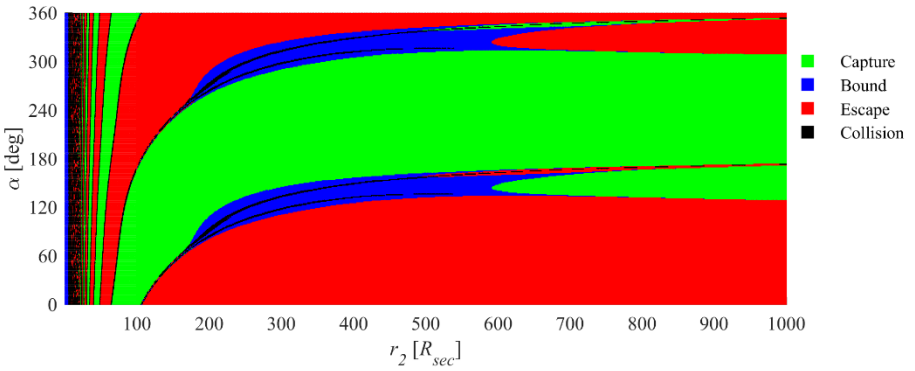

Figure 21. ICM for the prograde case with $\mu = \mu_3$ and q=20.

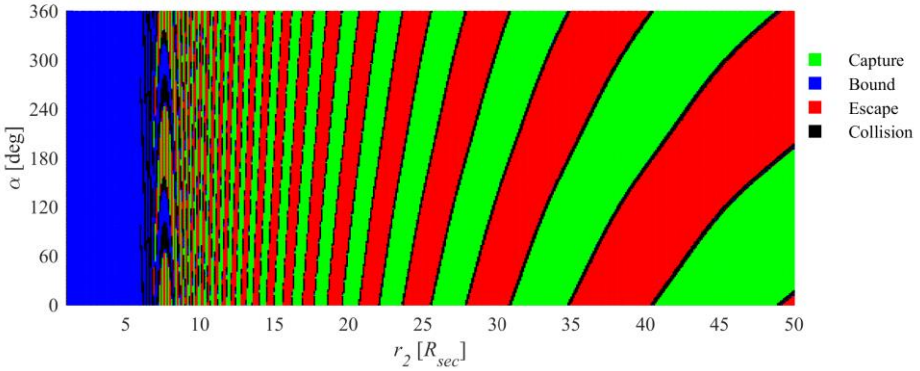

Figure 22. ICM (zoomed in) for the prograde case with $\mu = \mu_3$ and q=20.

For prograde motion, the ICMs with same the perigee radius have a similar structure in spite of the difference in mass ratio. Generally, based on the distribution of ICM regions in different colours, the structure of the ICM can be classified into three zones, an undisrupted zone (zone I), an irregular zone (zone II) and a regular zone (zone III). Based on Fig. 18, a schematic diagram is shown in Fig. 23 to illustrate the structure in ICM.

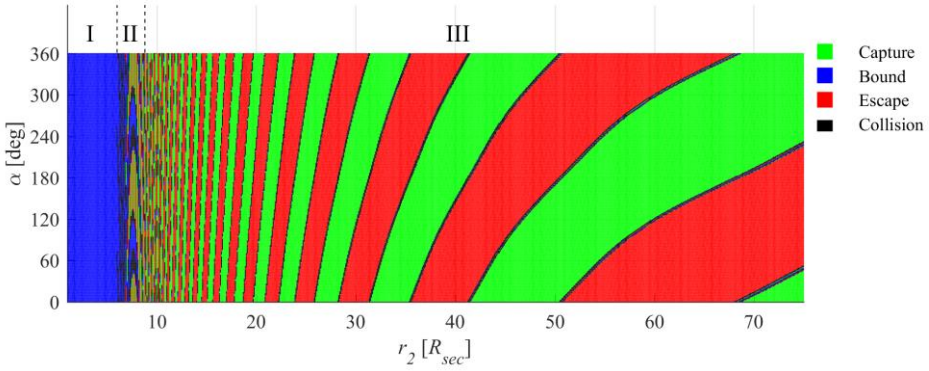

Figure 23. Schematic diagram for the structure in ICM

The undisrupted zone (zone I) is the layer of the ICM where P_3 is still in a bound orbit with respect to P_2 after the flyby around the central body. The size of the undisrupted zone is affected by the perigee radius q, which will shrink significantly with a smaller perigee radius, as seen in Figs. 14, 16, 18. However, the size of the undisrupted zone is seldom affected by the mass ratio, as seen in Figs. 18, 20, 22. The irregular zone (zone II) is the layer in which small changes to the initial conditions cause a significantly different evolution for P_3, represented as different classes of motions are which are closely packed in the ICMs. From numerical simulation, the upper limit for the irregular zone is approximately $r_2 \approx 10R_{sec}$. The regular zone is the area where different classes of motions are clearly distinguished, and in which the bound area will bifurcate twice at approximately 500~600R_{sec}. An interesting point is the behaviour at the boundaries between the capture, bound and escape regions. As collisions are taken into consideration in this paper, in a majority of prograde cases the boundaries are always collision regions. In References [48, 49], without considering collisions, the authors numerically demonstrated that the boundaries between different regions should be the invariant manifolds related to L_i^+, which trend to L_i as $t \to +\infty$. This point can provide further insights into the ICMs.

Among the capture cases, we select the orbits with the smallest semi-major axis with respect to the central body P_1, at the termination of the simulation. These are considered as the optimum results and the parameters for the optimum capture orbits for the prograde cases are listed in Table 1, which can primarily determine the scope of the related parameters in the binary pair for stable capture within the central body's SOI. All distances are again measured in units of the radius of the central body.

Table 1. Optimum Capture Orbits for Prograde Cases

	Semi-major axis			Eccentricity		
q	$\mu=\mu_1$	$\mu=\mu_2$	$\mu=\mu_3$	$\mu=\mu_1$	$\mu=\mu_2$	$\mu=\mu_3$

2	40.309615	404.38760	4043.6668	0.9511177	0.9950617	0.9995054
5	74.501841	743.02535	7416.7208	0.9334363	0.9932762	0.9993259
10	150.07599	1485.4269	14862.043	0.9339520	0.9932734	0.9993272
15	222.34111	2202.5038	21972.610	0.9330951	0.9931951	0.9993173
20	294.90607	3019.1924	30103.673	0.9327389	0.9933825	0.9993356

Some simple regularities can be summarized in Table 1. It can be seen that the semi-major axis a of the optimum capture orbit is approximately in proportion to the inverse cubic root of mass ratio μ and has an approximately linear relationship with the perigee radius q. Taking the data in the 1st row of Table 1 for example, values of $a\sqrt[3]{\mu}$ are found to be 0.451235, 0.452681 and 0.452658 respectively, which are almost constant and verify the inverse cubic root relationship. For the linear relationship with respect to perigee radius q, we take the data in the 1st column, for example, and the values of a/q are found to be 20.154808, 14.900368, 15.007599, 14.822741, 14.963774 respectively. Except for the first one, all results almost satisfy the linear relationship. Similarly, the eccentricity e of the optimum capture orbit is almost constant for different perigee radii q. Moreover, with the same perigee radius q, the term $1-e$, a modification of the eccentricity, is approximately in proportion to the cubic root of mass ratio μ.

These regularities can be understood through a simple analytical model. In Reference [44, 55], an approximation of the specific orbital energy ΔE for the disrupted particle is given as

$$|\Delta E| = \frac{Gm_1R_2}{R_t^2} \tag{29}$$

where G is the gravitational constant, m_1 is the mass of the central body P_1 and R_2 is the distance between the particle P_3 and the main asteroid P_2. Then R_t is the tidal radius, defined as

$$R_t = R_2\sqrt[3]{m_1/m_2} \approx R_2\sqrt[3]{1/\mu} \tag{30}$$

in which m_2 is the mass of the main asteroid P_2. Since the main asteroid P_2 is in a parabolic orbit with respect to the central body, the tidal radius R_t can also be rewritten as

$$R_t = \frac{2q}{1+cosf_t} \tag{31}$$

f_t is the true anomaly when P_2 enters the tidal radius of the central body P_1, which is constant. Therefore Eq. (31) can also be described by

$$R_t \propto 2q \tag{32}$$

Substituting Eq. (30) and Eq. (32) into the expression for ΔE yields

$$|\Delta E| \propto \frac{Gm_1}{2q\sqrt[3]{1/\mu}} \tag{33}$$

For a capture case with semi-major axis a, the orbital energy can also be represented as

$$\Delta E = -\frac{Gm_1}{2a} \tag{34}$$

Therefore, with a straightforward simplification, we can derive

$$a \propto q\sqrt[3]{1/\mu} \tag{35}$$

which verifies the aforementioned regularities related to the semi-major axis a.

For the eccentricity e, a similar analytical expression can also be derived. Substituting Eq. (30) into Eq. (29), we can derive $|\Delta E| = \mu\, Gm_1/R_t$, which yields

$$\frac{|\Delta E|}{E} \propto \mu \tag{36}$$

with E the potential energy for parabolic orbit. Since ΔE is much smaller than the potential energy E, we assume that the perigee radius q for the trajectory of P_3 is almost the same as the initial parabolic orbit, such that $q = a(1-e)$ is approximately constant. Substituting Eq. (35) into this relationship, it can be seen that

$$1 - e \propto \sqrt[3]{\mu} \tag{37}$$

which verifies the aforementioned regularities related to the eccentricity e.

Based on the above regularities, we can briefly determine some parameters of the PPRTBP for the prograde case from the constrains on the final capture orbit of P_3. For example, if we set the Earth as the central body P_1 and prescribe that the final capture orbit of P_3 should be within the Hill sphere of P_1 (almost 200 Earth radii) to remain bound under solar perturbations, then the feasible range for the perigee radius q and mass ratio μ should be chosen as $q \leq 7$ and $\mu \geq 10^{-7}$ for the prograde case. The feasible range of μ can also be verified through qualitative analysis; to ensure binary disruption, the orbital speed of the original binary system should be comparable to the encounter speed between the primaries [23]. Since the encounter speed of the parabolic orbit at the Earth is generally 10 kms^{-1}, the mass of P_2 is required to be relatively large (with a mass ratio of order 10^{-6}~10^{-7} corresponding to a radius of 40~100km) to ensure that the orbital speed of P_3 is in the correct range [35]. Although a large main asteroid is required (with radius larger than 40 km) for permanent capture within the Earth's Hill sphere, the required size of the binary asteroid can be reduced. Through dimensional analysis, if the central body is chosen as the Moon, it is feasible to generate a stable capture with a main asteroid radius of order 10 km. Methods to increase the potential energy between the binary pair, such as a tethered binary system [56], can also increase the feasibility of capture with smaller binary asteroids. These methods will be investigated in further research.

For the retrograde orbits, ICMs with the same parameters as the prograde case are shown in Figs 24-30 for completeness.

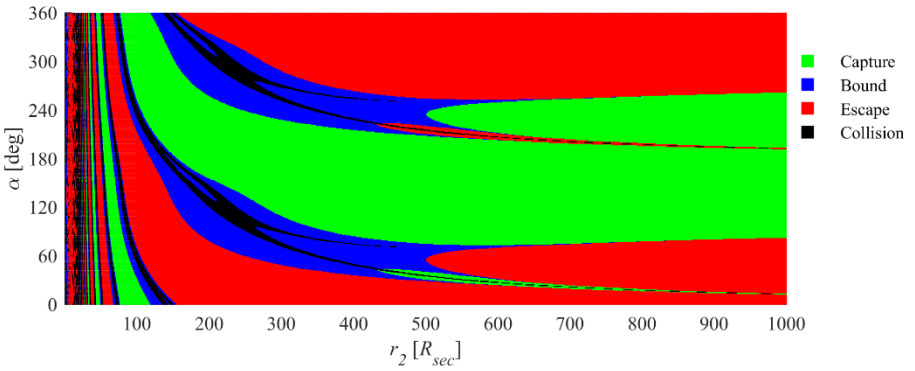

Figure 24. ICM for the retrograde case with $\mu = \mu_2$ and q=2.

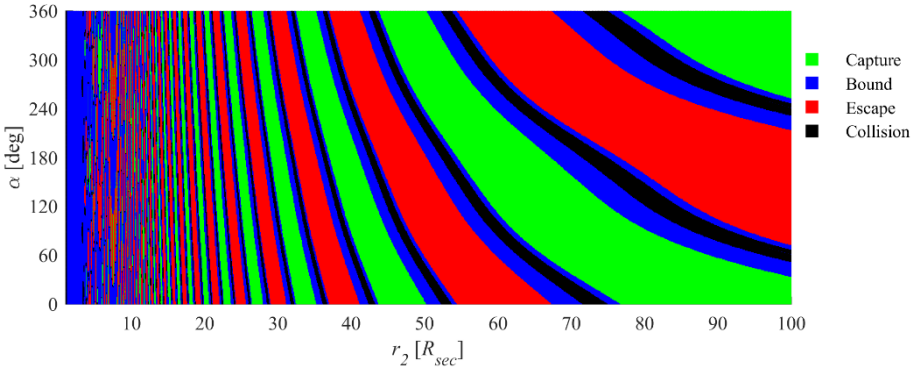

Figure 25. ICM (zoomed in) for the retrograde case with $\mu = \mu_2$ and q=2.

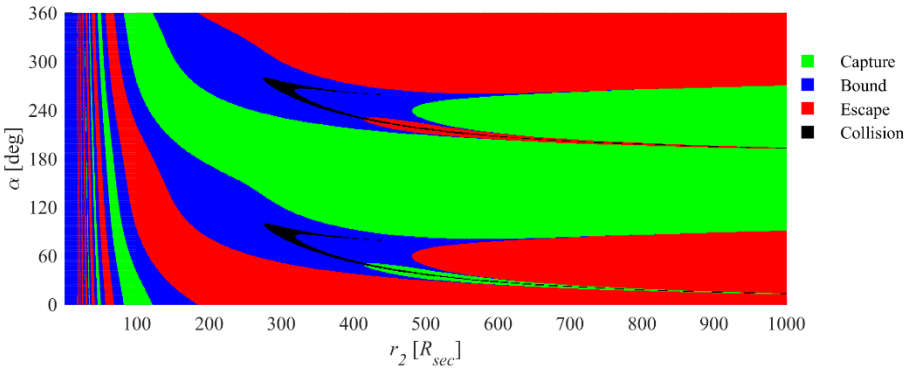

Figure 26. ICM for the retrograde case with $\mu = \mu_2$ and q=10.

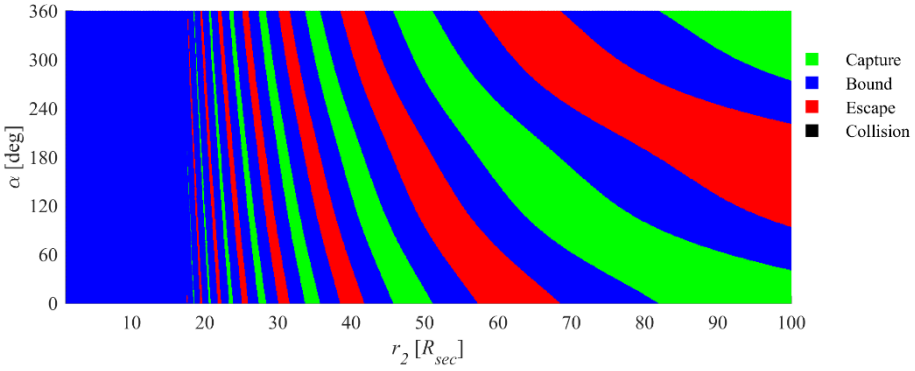

Figure 27. ICM (zoomed in) for the retrograde case with $\mu = \mu_2$ and q=10.

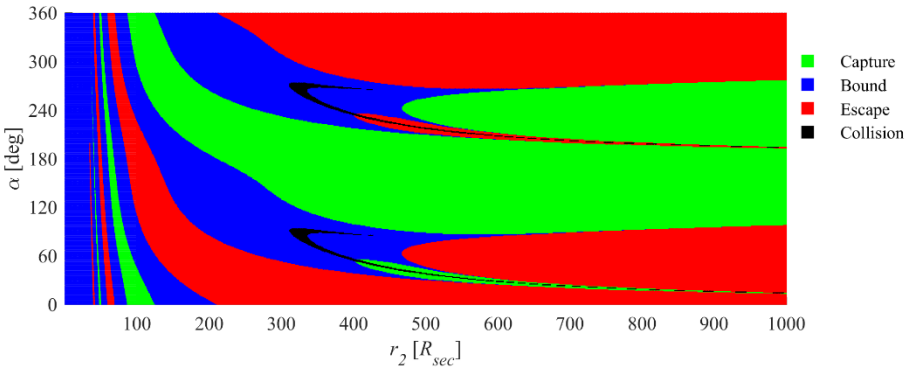

Figure 28. ICM for the retrograde case with $\mu = \mu_2$ and q=20.

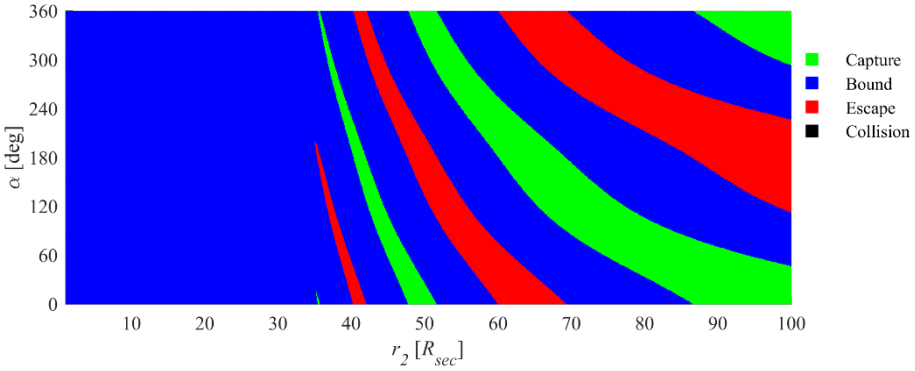

Figure 29. ICM (zoomed in) for the retrograde case with $\mu = \mu_2$ and q=20.

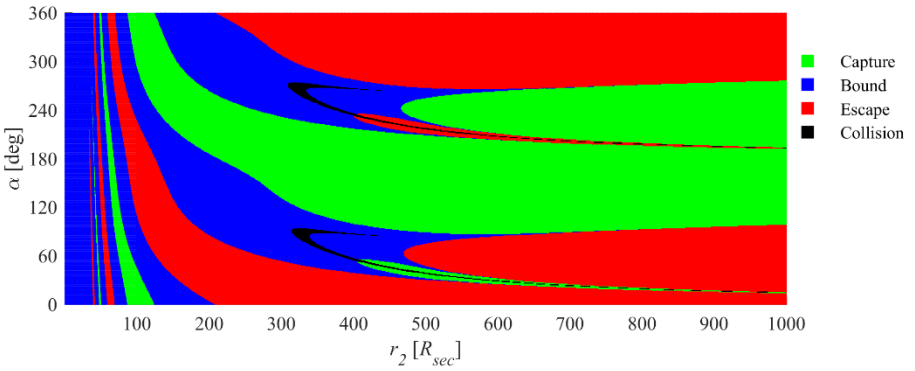

Figure 30. ICM for the retrograde case with $\mu = \mu_1$ and q=20.

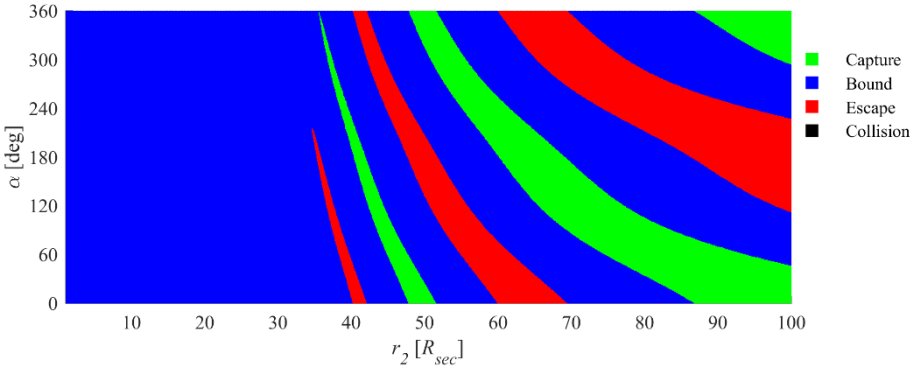

Figure 31. ICM (zoomed in) for the retrograde case with $\mu = \mu_1$ and q=20.

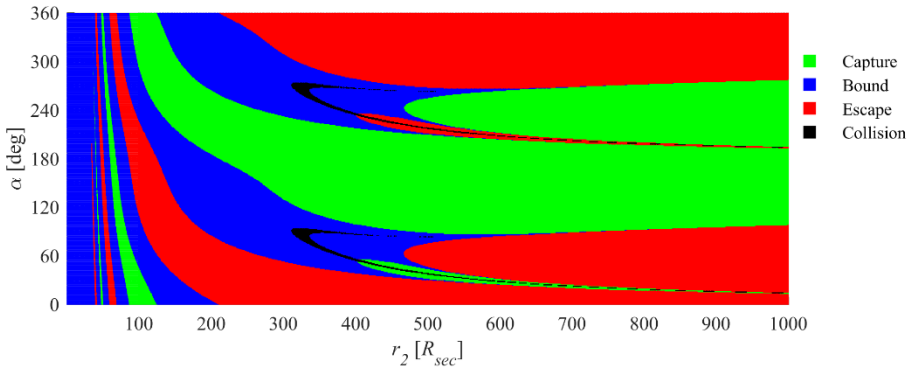

Figure 32. ICM for the retrograde case with $\mu = \mu_3$ and q=20.

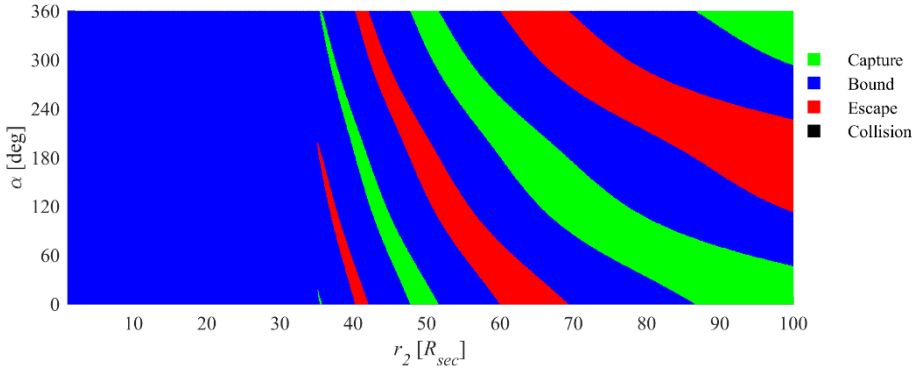

Figure 33. ICM (zoomed in) for the retrograde case with $\mu = \mu_3$ and q=20.

Clearly, the retrograde problem has similar characters to the prograde case. Moreover, with the same parameters, retrograde orbits always have a larger undisrupted zone, which means that retrograde orbits are more stable, compared with the prograde orbits. For the retrograde case, the parameters for the optimum capture orbits are listed in Table 2.

Table 2. Optimum Capture Orbits for Retrograde Cases

	Semi-major axis			Eccentricity		
q	$\mu=\mu_1$	$\mu=\mu_2$	$\mu=\mu_3$	$\mu=\mu_1$	$\mu=\mu_2$	$\mu=\mu_3$
2	721.05422	7068.7595	70548.095	0.9970436	0.9997152	0.9999716
5	1797.9728	17618.684	175834.79	0.9970325	0.9997143	0.9999715
10	3519.4415	34490.992	344224.84	0.9969551	0.9997080	0.9999709
15	5260.6750	51503.156	513957.95	0.9969506	0.9997067	0.9999707
20	6999.1735	68634.709	685011.68	0.9969338	0.9997065	0.9999708

As with the prograde case, similar regularities can also be summarized in Table 2 for the retrograde case. For conciseness, we will not repeat them again. Note that it is easy to find, with the same sets of parameters, the semi-major axis and eccentricity of the optimum capture orbits in the retrograde case which are always much larger than those of the prograde case. This also implies that the retrograde case is more stable and difficult to disrupt, compared with the prograde case, as expected. For this reason, the prograde case should be chosen for the artificial capture of binary asteroids.

To verify the linear analysis based on Eq. (16), we consider the statistics of the capture cases from numerical simulation to determine whether they satisfy the critical value of the Jacobi function, which was derived from the linear model. The relative error for the statistics of the capture cases is now defined as

$$Err_{rlt} = \frac{A_{uns\_c}}{A_{tot\_c}} \approx \frac{\sum w_{uns\_c} N_{uns\_c}}{\sum (w_{uns\_c} N_{uns\_c} + w_{sat\_c} N_{sat\_c})} \tag{38}$$

where A_{unsat_c} is the area of the capture region of the ICM which does not satisfy the critical value of Jacobi function and A_{tot_c} is the total area of capture region in the ICM. As Eq. (28) shows, the probe points for the simulation are discrete and the sampling density also varies in different zones of the ICM. For this reason, we adopt a weighted arithmetic mean to approximate the area ratio, with weight w_{uns_c} and number N_{uns_c} representing the density and number of probe points in capture region which do not satisfy the critical value of the Jacobi function. Similarly, the weight w_{sat_c} and number N_{sat_c} represent the density and number of probe points in capture region which satisfy the critical value of the Jacobi function. From the simulation results above, the maximum deviation of Err_{rlt} is always less than 1.7%, which verifies the quality of the approximation represented by the linear model.

6 Engineering the Capture of Binary Asteroids

As discussed earlier, besides the capture region, the ICM also consists of a bound region, an escape region and a collision region. Therefore, for the artificial capture of binary asteroids, the improvement of the capture ratio is a key issue, by engineering the boundaries of these regions. In this section, two strategies will now be investigated to engineer and expand the capture region. Again, we note that a large primary asteroid is in general required; however, the analysis provides new insights into the asteroid capture problem and can be scaled to other bodies.

6.1 Re-phasing manoeuvres

The ICMs discussed in Section 5 illustrate the capture region in the space of initial conditions. Therefore, to ensure that capture occurs, the particle P_3 can in principle be manoeuvred into the capture region when the binary enters the fixed disk about the central body representing the starting point for numerical integration of the ICMs. A potential strategy to improve capture probability is therefore a re-phasing manoeuvre, which is a two-impulse Hohmann transfer from and back to the same orbit [57]. This manoeuvre is used to rephrase the position of the minor asteroid relative to the main asteroid, without changing the orbital radius, which will ensure the particle falls in the capture region (with the same r_2) of the ICM when the binary enters the initial fixed disk.

Here we will take the bound case in Section 5.1 as an example for illustration. Around the example point, a zoomed-in ICM is presented in Fig. 34. For the target point to transfer to, we randomly choose the closest capture point in the ICM with the same r_2, shown in Fig. 34 with the green label. We assume a re-phasing manoeuvre is executed, which changes the phase angle of the example point from $\alpha = 78^\circ$ to $\alpha = 86^\circ$ when the binary pair enters the initial fixed disk for ICM. The trajectories for the original motion and the re-phased motion are presented in Fig. 35, where a bound case has been engineered into a capture case.

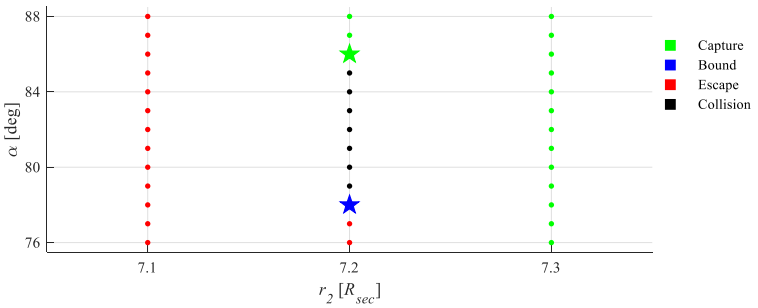

Figure 34. Zoomed-in ICM around example point.
Blue label: example point. Green label: target point.

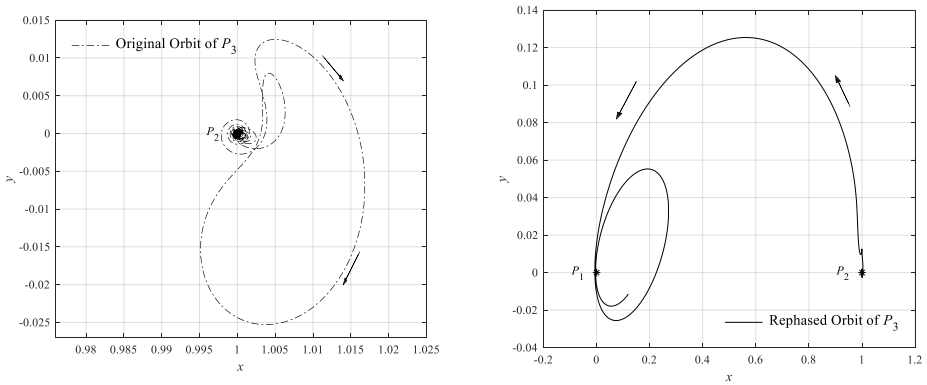

Figure 35. Orbits for original and re-phrased motions. Left: Original. Right: Re-phased.

As noted, the re-phasing manoeuvre will maintain the same orbit radius after the re-phasing manoeuvre. Therefore, for a given r_2, if only one capture point exits with radius r_2 in the ICM, all other points along the column with r_2 in the ICM, can be re-phased as capture cases, which extends the capture area of the ICM. Similar to Eq. (38), through the area ratio between the capture regions (green) and the entire ICM, we can calculate the capture ratio with/without re-phasing manoeuvre. A comparison for the capture ratio of all data (12,150,000 simulations in total) between the original results and the re-phased results is then shown in Table 3 and Table 4 for prograde orbits and retrograde orbits respectively. It can be seen that, in both the prograde and retrograde cases, the re-phasing manoeuvre can dramatically increase the possibility of capture.

Table 3. Comparison for capture probability in prograde orbit

	Original Case			Re-phasing Manoeuvre Case		
q	$\mu=\mu_1$	$\mu=\mu_2$	$\mu=\mu_3$	$\mu=\mu_1$	$\mu=\mu_2$	$\mu=\mu_3$
2	36.0014%	44.3375%	44.3592%	100.000%	100.000%	100.000%
5	44.6026%	44.8257%	44.8466%	99.9399%	99.9299%	99.9299%
10	44.9030%	45.1256%	45.1573%	99.7697%	99.7597%	99.7598%
15	45.0516%	45.2928%	45.3134%	99.5996%	99.5895%	99.5896%
20	45.1438%	45.3772%	45.3985%	99.4294%	99.4194%	99.4194%

Table 4. Comparison for capture probability in retrograde orbit

	Original Case			Re-phasing Manoeuvre Case		
q	$\mu=\mu_1$	$\mu=\mu_2$	$\mu=\mu_3$	$\mu=\mu_1$	$\mu=\mu_2$	$\mu=\mu_3$
2	39.7239%	41.4702%	41.4919%	99.7497%	99.7497%	99.7497%
5	40.3564%	40.6133%	40.6375%	99.2192%	99.2292%	99.2292%
10	39.3705%	39.6435%	39.6616%	98.3984%	98.3984%	98.3984%
15	38.5750%	38.8477%	38.8672%	97.4975%	97.4975%	97.4975%
20	37.8951%	38.1570%	38.1832%	96.5966%	96.5966%	96.5966%

Since the re-phasing manoeuvre occurs far from the central body, whose perturbation can be neglected, a two-body model can be adopted for preliminary analysis. In the two-body model, the magnitude of the Δv required for the re-phasing manoeuvre for the initially circular orbit can be defined as

$$\Delta v = 2\left|\sqrt{\frac{Gm_2}{|\mathbf{R}_2|}} - \sqrt{\frac{2Gm_2}{|\mathbf{R}_2|} - \frac{Gm_2}{a_{trf}}}\right| \tag{39}$$

in which a_{trf} is the semi-major axis of the elliptical transfer orbit for the re-phasing manoeuvre in the inertial frame, which satisfies $a_{trf} \in [|\mathbf{R}_2|/2, +\infty)$. From Eq. (39), it can be seen that, when $a_{trf} = |\mathbf{R}_2|$, $\Delta v = 0$, which is minimum. Therefore, for any small positive value of Δv, mathematically there exists an a_{trf} such that the re-phasing manoeuvre can occur, while at the cost of increased transfer time. In principle, an infinitesimal Δv is required as the transfer time increases without bound. Physically, the phase angle and transfer time should be specified for the re-phasing manoeuvre, and then the Δv will be determined under these constrains. Moreover, it should also be noted that for engineering applications, some practical constrains (such as the energy cost of reaching the binary asteroid early) must be taken into consideration when considering the re-phasing manoeuvre, which is out of the scope of this paper.

6.2 Optimal single-impulse transfer for capture

It is clear that the PPRTBP is highly nonlinear and the final evolution of the binary pair is extremely sensitive to the initial conditions. Since we are considering engineering of the capture dynamics, we now propose another strategy for capture that leverages the non-linearity of the problem for manoeuvres within the initial disk of the ICMs. In this strategy, we apply a small impulsive manoeuvre Δv to the particle P_3 and then use an optimisation algorithm to minimize the magnitude of Δv required to transfer P_3 from being a bound case to a capture case. This then ensures that P_3 is trapped within the appropriate ZVC after the fly-by.

To verify the feasibility of this strategy, we consider a scenario to capture P_3 through an optimal single-impulse transfer. The point along the parabolic orbit at which the impulse is implemented for the transfer is fixed in this example scenario for simplification. The parameters are chosen as $\mu = 1.40276 \times 10^{-6}$, $k = 7.6$, $\alpha = 274^\circ$ and $q = 2$. The point at which the impulse is implemented is set as $f = -107.5^\circ$ ($\theta = f/2 = -53.75^\circ$). The terminal eccentricity e_{trm} of P_3 with respect to P_1, in the inertial frame, is chosen as the constrain for optimization. Considering the distribution of eccentricity in Table 1, the range for e_{trm} is set

as $e_{trm}\epsilon[0.9, 0.999]$. Utilizing the *fmincon* function in MATLAB with *TolCon* = 1x10^{-7} and *TolX* = 1x10^{-14}, the optimized transfer orbit can then be obtained. The minimized modulus of Δv is found to be 2.67×10^{-4} in non-dimensional units. The optimized transfer is shown in Fig. 36, in which the red star indicates the point at which the required Δv is implemented.

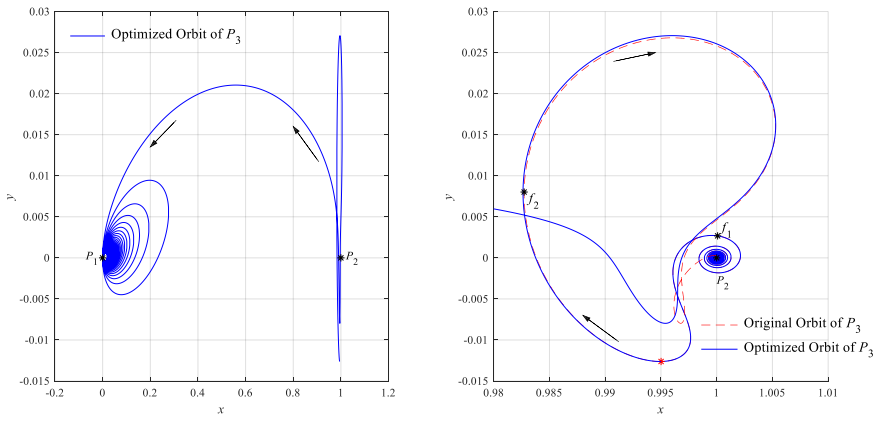

Figure 36. Optimized capture orbit of P_3. Left: Zoomed Out. Right: Zoomed In.

Along the same trajectory described above, if we relocate the impulse point, we can obtain a series of optimized results at different true anomalies. For illustration, the original bound trajectory is now divided into three segments separated by two black asterisk points f_1 and f_2 as shown in Fig. 36, whose true anomalies correspond to $f_1 = -156^\circ$ and $f_2 = -40^\circ$ respectively. Clearly, the segment 1, with $f \leq -156^\circ$, represents the phase when the binary pair has not been disrupted. Then segment 2, with $-156^\circ \leq f \leq -40^\circ$, shows the phase when the particle P_3 has temporarily escaped from its orbit around P_2 and coasts to the furthest distance from P_2. Finally, the segment 3, with $f \geq -40^\circ$, is the phase when the particle P_3 returns to P_2, again captured by the main asteroid. Since we are clearly interested in transfers with a small Δv, segment 2 is then chosen for optimization. The optimized results are presented in Fig. 37, which illustrate the magnitude of the Δv in non-dimensional units and SI units (set with the Earth as the central body) with respect to f ranging from -156° to -40°.

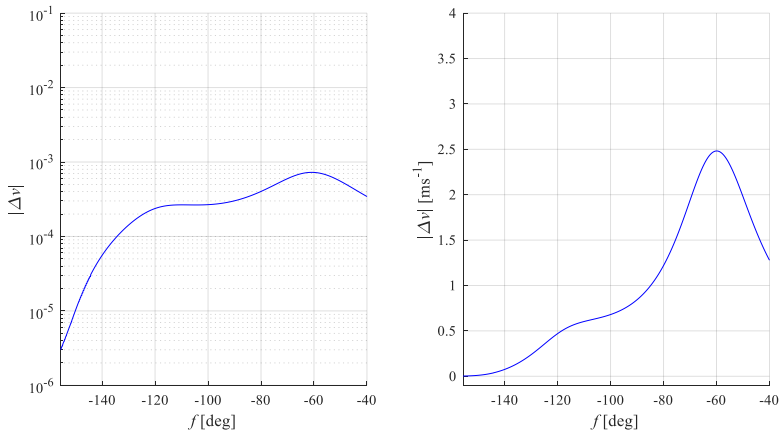

Figure 37. Magnitude of optimized Δv. Left: Non-dimensional Units. Right: SI Units.

For the other two segments of trajectory, we can provide a brief analysis of the Δv (or energy) required for a single-impulse transfer. For segment 1 with $f < -156^{\circ}$, the particle is still in a bound orbit around P_2 and the binary pair is far from the central body, so that the perturbation of P_1 is small. Neglecting the weak perturbation, it can be treated as a two-body problem for simplification. Therefore, the Δv that particle P_3 requires would be negligible, compared with the orbital energy of P_2 with respect to P_1. This point can also be verified by the gradient of the curve for f close to -150° in Fig. 33. For the segment with $f > -40^{\circ}$, the particle P_3 has reached the furthest distance from P_2 and then returns to P_2. Clearly, it will require a large Δv to manoeuvre its orbit relative to the central body P_1 for capture. This coarse analysis is also verified by numerical simulation that there exists a limit on the true anomaly f for the optimal single-impulse transfer, at approximately $f \approx -38^{\circ}$. When f is larger than this critical value, no feasible optimal results can be obtained. Due to this phenomenon, since the singularities have been eliminated, it is inferred that, close to pericentre, single-impulse manoeuvres may not be feasible. Another inference is that solutions may exist, but will require more sophisticated numerical methods, which will not be pursued here. No matter, since the physical nature of the problem tells us to use a manoeuvre at a large distance from the pericentre to minimize the required Δv (approximating the re-phrasing manoeuvre at infinity from the previous section), we will only consider the segment with $f < -40^{\circ}$ to engineer the capture of the minor asteroid of the binary asteroid pair. Moreover, it should also be noted that the variation of Δv may depend on different zones in the ICM. Currently, we are planning some further explorations in this point.

7 Conclusions

In this paper, we have investigated the feasibility of capturing one member of a binary asteroid pair through disruption of the binary asteroid during the flyby of a central body, e.g. the Earth. To reduce the complexity of the problem, we adopted the planar parabolic restricted three-body problem for simplification and derived a set of related regularised equations of motion. Based on the planar parabolic restricted three-body problem, we also conducted a linear analysis for motion of the minor asteroid of the binary pair, assumed to be a particle, and derived a value of the critical Jacobi function required for disruption. To verify the validity of the analytical result, we implemented a numerical simulation and a statistical analysis which demonstrated that more than 98.3% of results satisfy the critical value of the Jacobi function found.

The simulation results also allow the motion of the particle to be classified as capture, bound and escape. Several numerical examples have been provided to illustrate the underlying dynamics of these three types of motion through the topology of the zero velocity curves. The initial condition maps for the evolution of particles determine the capture region in the initial configuration space. Two strategies have then been proposed to investigate the possibility of engineering the capture process. One is a re-phasing manoeuvre before encounter to engineer the initial condition maps, the other is an optimal single-impulse transfer during encounter. Using the optimal single-impulse transfer, it is feasible to change the particle's evolution from a bound case to a capture case prior to the flyby of the central body, ensuring that the minor asteroid is trapped within the correct zero velocity curve.

Based on the numerical results, to capture an asteroid through binary-asteroid disruption around the Earth, the radius of the main asteroid should be approximately 40~100 km to ensure a stable capture within the Earth's Hill sphere. This size will decrease to approximately 10 km, if the Moon is chosen as the central body. While a large main asteroid is required (to ensure sufficient gravitational binding energy which can be exchanged during the flyby), the analysis provides insights into the capture process, an accurate assessment of the Jacobi function required for capture and detailed initial condition maps which can then be used to develop strategies which can in principle engineer the capture process. We note that the binding gravitational energy of binary pair could in principle be enhanced through electrostatic charging, or an elastic tether, to reduce the size of the main asteroid body required for the capture of binary asteroid investigated.

Acknowledgments

We acknowledge support through the China Scholarship Council (XL) and a Royal Society Wolfson Research Merit Award (CM).

References

[1] DeMeo, F.E., Carry. B.: Solar System evolution from compositional mapping of the asteroid belt. Nature. 505(7485), 629-634 (2014)

[2] Edgeworth, K.E.: The origin and evolution of the solar system. Mon. Not. R. Astron. Soc. 109(5), 600-609 (1949)

[3] Ball, A.J., Ulamec, S., Dachwald, B., et al.: A small mission for in situ exploration of a primitive binary near-Earth asteroid. Adv. Space Res. 43(2), 317-324 (1999)

[4] Michel, P., DeMeo, F.E., Bottke. W.F.: Asteroids: Recent Advances and New Perspectives. Asteroids IV, pp. 3-10. University of Arizona Press, Tuscon (2015)

[5] European Space Agency.: Cosmic Vision: Space Science for Europe 2015-2025. 1-11. ESA Publications Division, Noordwijk (2005)

[6] Space Studies Board, National Research Council, et al.: Vision and voyages for planetary science in the decade 2013-2022. National Academies Press, Washington (2012)

[7] Sonter, M.: Near earth objects as resources for space industrialization. Solar System Development Journal. 1, 1-31 (2001)

[8] Elvis, M.: Let's mine asteroids-for science and profit. Nature. 485(7400), 549 (2012)

[9] Mazanek, D.D., Merrill, R.G., Brophy, J.R., et al.: Asteroid redirect mission concept: a bold approach for utilizing space resources. Acta Astronautica. 117, 163-171 (2015)

[10] Meinert, L.D., Robinson, G.R., Nassar, N.T.: Mineral Resources: Reserves, Peak Production and the Future. Resources. 5(1), 1-14 (2016)

[11] Chapman, C.R.: The hazard of near-Earth asteroid impacts on earth. Earth Planet. Sci. Lett. 222(1), 1-15 (2004)

[12] Pascale, P.D., Vasile, M., Casotto, S.: Optimal options for rendezvous and impact missions to NEOs. J. Br. Interplanet. Soc. 59(11), 386-394 (2006)

[13] Kawaguchi, J., Fujiwara, A., Uesugi, T.: Hayabusa—Its technology and science accomplishment summary and Hayabusa-2. Acta Astronautica. 62(10), 639-647 (2008)

[14] A'Hearn, M.F., Belton, M.J.S., Delamere, W.A., et al.: Deep impact: excavating comet Tempel 1. Science. 310(5746), 258-264 (2005)

[15] Scheeres, D.J., Marzari, F., Tomasella, L., et al: ROSETTA mission: satellite orbits around a cometary nucleus. Planet. Space Sci. 46(6), 649-671 (1998)

[16] Brophy, J.R., Friedman, L., Culick, F.: Asteroid retrieval feasibility. In: Aerospace Conference, 2012 IEEE, pp. 1-16. IEEE (2012)
[17] Hasnain, Z., Lamb, C.A., Ross, S.D.: Capturing near-Earth asteroids around Earth. Acta Astronautica. 81(2), 523-531 (2012)
[18] Baoyin, H.X., Chen, Y., Li, J.F.: Capturing near earth objects. Res. Astron. Astrophys. 10(6), 587-598 (2010)
[19] Urrutxua, H., Scheers, D.J., Bombardelli, C.: What does it take to capture an Asteroid? A case study on capturing Asteroid 2006 RH120. In 24th AAS/AIAA Space Flight Mechanics Meeting, Santa Fe, New Mexico. 2014.
[20] Belbruno, E., Gidea, M., Topputo, F.: Weak stability boundary and invariant manifolds. SIAM J. Appl. Dyn. Syst. 9(3), 1061-1089 (2010)
[21] Yárnoz, D.G., Sanchez, J.P., McInnes, C.R.: Easily retrievable objects among the NEO population. Celest. Mech. Dyn. Astron. 116(4), 367-388 (2013)
[22] Tan. M.H., McInnes, C.R., Ceriotti, M.: Direct and indirect capture of near-Earth asteroids in the Earth-Moon system. Celest. Mech. Dyn. Astron. 129(1-2), 57-88 (2017)
[23] Agnor, C.B., Hamilton, D.P.: Neptune's capture of its moon Triton in a binary–planet gravitational encounter. Nature. 441(7090), 192-194 (2006)
[24] Neto, E.V., Winter, O.C.: Gravitational Capture of Asteroids by Gas Drag. Math. Probl. Eng. 2009 (2010)
[25] Pollack, J.B., Burns, J.A., Tauber, M.E.: Gas drag in primordial circumplanetary envelopes: A mechanism for satellite capture. Icarus. 37(3), 587-611 (1979)
[26] Heppenheimer, T.A., Porco, P.: New contributions to the problem of capture. Icarus. 30(2), 385-401 (1977)
[27] Sanchez, J.P., McInnes, C.R.: Synergistic approach of asteroid exploitation and planetary protection. Adv. Space Res. 49(4), 667-685 (2012)
[28] Moorhead, A.V., Cooke, W.J.: Enhancement of the natural Earth satellite population through meteoroid aerocapture. In: AAS/Division of Dynamical Astronomy Meeting, #45, id.103.03 (2014)
[29] Gong, S.P., Li, M.: Satellite capture mechanism in a sun-planet-binary four-body system. Astrophys. Space Sci. 362(2), 40-53 (2017)
[30] Philpott, C.M., Hamilton, D.P., Agnor. C.B.: Three-body capture of irregular satellites: Application to Jupiter. Icarus. 208(2), 824-836 (2010)
[31] Astakhov, S.A., Burbanks, A.D., Wiggins, S., et al: Chaos-assisted capture of irregular moons. Nature. 423(6937), 264-267 (2003)
[32] Astakhov, S.A., Farrelly, D.: Capture and escape in the elliptic restricted three‐body problem. Mon. Not. R. Astron. Soc. 354(4), 971-979 (2004)
[33] Verrier, P.E., McInnes, C.R.: Low-Energy Capture of Asteroids onto Kolmogorov–Arnold–Moser Tori. J. Guid.Control Dynam. 38(2), 330-335 (2014)
[34] Tanikawa, K.: Impossibility of the capture of retrograde satellites in the restricted three-body problem. Celestial mechanics. 29(4), 367-402 (1983)
[35] Nesvorný, D., Vokrouhlický, D., Morbidelli, A.: Capture of irregular satellites during planetary encounters. Astron. J. 133(5), 1962-1976 (2007)
[36] Chapman, C.R., Veverka, J., Thomas, P.C., et al.: Discovery and physical properties of Dactyl, a satellite of asteroid 243 Ida. Nature. 374(6525), 783-784 (1995)
[37] Belton, M.J.S., Chapman, C.R., Thomas, P.C., et al.: Bulk density of asteroid 243 Ida from the orbit of its satellite Dactyl. Nature. 374(6525), 785-788 (1995)
[38] Weidenschilling, S.J., Paolicchi, P., Zappala, V.: Do asteroids have satellites? Asteroids II, pp. 643-660. University of Arizona Press, Tuscon (1989)

[39] Merline, W.J., Weidenschilling, S.J., Durda, D.D., et al.: Asteroids do have satellites. Asteroids III, pp. 289-312. University of Arizona Press, Tuscon (2002)
[40] Bottke, W.F., Melosh, H.J.: Binary asteroids and the formation of doublet craters. Icarus. 124(2), 372-391 (1996)
[41] Gaspar, H.S., Winter, O.C., Neto, E.V.: Irregular satellites of Jupiter: capture configurations of binary-asteroids. Mon. Not. R. Astron. Soc. 415(3), 1999-2008 (2011)
[42] Gaspar, H.S., Winter, O.C., Neto, E.V.: Irregular satellites of Jupiter: three-dimensional study of binary-asteroid captures. Mon. Not. R. Astron. Soc. 433(1), 36-46 (2013)
[43] Borum, A., Burns, J., Wentzel, P., et al.: Capturing Near-Earth asteroids using a binary exchange mechanism. In: Virginia Space Grant Consortium Student Research Conference, Williamsburg (2012)
[44] Sari, R., Kobayashi, S., Rossi, E.M.: Hypervelocity Stars and the Restricted Parabolic Three-Body Problem. Astrophys. J. 708(1), 605-614 (2009)
[45] Kanaan, W., Farrelly, D., Lanchares, V.: Satellite capture as a restricted 2+2 body problem. Adv. Space Res. 61(8), 2124-2134 (2018)
[46] Alvarez, M., Delgado, J., Cors, J.M.: Exchange and capture in the planar restricted parabolic 3-body problem. New Advances in Celestial Mechanics and Hamiltonian Systems, pp. 1-28. Springer, New York (2004)
[47] Alvarez, M., Cors, J.M., Delgado, J.; On final evolutions in the restricted planar parabolic three-body problem. Periodic, Quasi-Periodic and Chaotic Motions in Celestial Mechanics: Theory and Applications, pp. 173-200. Springer, Dordrecht (2006)
[48] Barrabés, E., Cors, J.M., Ollé, M.: Dynamics of the parabolic restricted three-body problem. Commun. Nonlinear Sci. Numer. Simulat. 29(1), 400-415 (2015)
[49] Barrabés, E., Cors, J.M., Garcia-Taberner, L., et al.: Tails and bridges in the parabolic restricted three-body problem. Mon. Not. R. Astron. Soc. 472(3), 2554-2568 (2017)
[50] Levi-Civita, T.: Sur la régularisation du probleme des trois corps. Acta Math. 42(1), 99-144 (1920)
[51] Koon, W.S., Lo, M.W., Marsden, J.E., et al.: Dynamical systems, the three-body problem and space mission design. Springer, New York (2007)
[52] Toomre, A., Toomre, J.: Galactic bridges and tails. Astrophys. J. 178, 623-666 (1972)
[53] Carry, B.: Density of asteroids. Planet. Space Sci. 73(1), 98-118 (2012)
[54] Araujo, R.A.N., Winter, O.C.: Near-Earth asteroid binaries in close encounters with the Earth. Astronomy & Astrophysics. 566, 1-10 (2014)
[55] Stone, N., Sari, R., Loeb, A.: Consequences of strong compression in tidal disruption events. Mon. Not. R. Astron. Soc. 435(3), 1809-1824 (2013)
[56] Sun, Q.L., Liu, Y.F., Qi, N.M., et al.: Dynamics of motorized momentum exchange tether for payloads capture. Adv. Space Res. 59(9), 2374-2388 (2017)
[57] Curtis, H.D.: Orbital mechanics for engineering students, 3rd ed. Butterworth-Heinemann, Waltham (2013)